ASTROBIOLOGY
Volume 22, Number 6, 2022

DOI: 10.1089/ast.2021.0126

Inefficient Water Degassing Inhibits Ocean Formation on Rocky Planets: An Insight from Self-Consistent Mantle Degassing Models

Yoshinori Miyazaki[1,2] and Jun Korenaga[1]

Abstract

A sufficient amount of water is required at the surface to develop water oceans. A significant fraction of water, however, remains in the mantle during magma ocean solidification, and thus the existence of water oceans is not guaranteed even for exoplanets located in the habitable zone. To discuss the likelihood of ocean formation, we built two models to predict the rate of mantle degassing during the magma ocean stage and the subsequent solid-state convection stage. We find that planets with low H_2O/CO_2 ratios would not have a sufficient amount of surface water to develop water oceans immediately after magma ocean solidification, and the majority of the water inventory would be retained in the mantle during their subsequent evolution regardless of planetary size. This is because oceanless planets are likely to operate under stagnant lid convection, and for such planets, dehydration stiffening of the depleted lithospheric mantle would limit the rate of mantle degassing. In contrast, a significant fraction of CO_2 would already be degassed during magma ocean solidification. With a strong greenhouse effect, all surface water would exist as vapor, and water oceans may be absent throughout planetary evolution. Volatile concentrations in the bulk silicate Earth are close to the threshold amount for ocean formation, so if Venus shared similar concentrations, small differences in solar radiation may explain the divergent evolutionary paths of Earth and Venus. Key Words: Habitability—Magma ocean—Ocean formation. Astrobiology 22, 713–734.

1. Introduction

The continuing discovery of extrasolar terrestrial planets has increased the prospect of identifying habitable exoplanets. Earth-size exoplanets are starting to be found at a heliocentric distance where liquid water may be stable (Gillon *et al.*, 2017; Gilbert *et al.*, 2020), and one of the super-Earth-size exoplanets identified in the habitable zone, K2-18b, has water vapor detected in its atmosphere (Benneke *et al.*, 2019b; Tsiaras *et al.*, 2019). With the upcoming James Webb Space Telescope, more detections of water vapor are expected on potentially habitable exoplanets (Gardner *et al.*, 2006), and the possible presence of surface water makes such exoplanets a leading candidate to search for biosignatures (Schulze-Makuch *et al.*, 2011; Madhusudhan *et al.*, 2020). Given the importance of surface water, one of the key questions is the likelihood of water ocean formation on a rocky exoplanet with a water vapor atmosphere.

The presence of surface water has often been discussed in terms of the habitable zone (Kasting *et al.*, 1993; Kopparapu *et al.*, 2013; Kodama *et al.*, 2019), which is the region where liquid water is stable at the temperature and pressure conditions of a planetary surface. The premise, however, is that the amount of surface water is large enough to develop oceans. Although a threshold value to form water oceans is $\sim 10^{16}$ kg for the present-day Earth and is thus well smaller than the current ocean mass (1.4×10^{21} kg), the threshold changes with the amount of greenhouse gases and net stellar radiation (Abe, 1993a; Salvador *et al.*, 2017). For example,

[1]Department of Earth and Planetary Sciences, Yale University, New Haven, Connecticut, USA.
[2]Division of Geological and Planetary Sciences, California Institute of Technology, Pasadena, California, USA.

during the early Hadean on Earth, an atmosphere of 100 bar CO_2 would have increased this threshold to $\sim$0.1 ocean mass, so it is not guaranteed that the threshold amount of water would always exist on the surface of terrestrial planets. A significant fraction of the water inventory can be retained in the planetary interior, precluding the formation of water oceans.

The initial amount of surface water is determined by volatile partitioning during magma ocean solidification, whereas its subsequent evolution is governed by interaction with mantle convection (Ito *et al.*, 1983; Korenaga *et al.*, 2017). Previous studies have often assumed that the mantle entirely degases during magma ocean solidification (Elkins-Tanton, 2008; Lebrun *et al.*, 2013; Salvador *et al.*, 2017), but considering the rheological transition of a partially molten medium and its slow compaction rate, a significant amount of volatiles could be trapped in the mantle (Hier-Majumder and Hirschmann, 2017).

Furthermore, if water oceans are initially absent, the lack of surface water may have persisted for a geological timescale. The presence of surface water is critical in reducing the lithospheric strength and thus in triggering plate tectonics (Korenaga, 2007, 2010a, 2020). Without oceans, the mantle would operate under stagnant lid convection, and mantle upwelling would be suppressed by a rigid lid covering the entire surface (Solomatov, 1995). Furthermore, dehydration stiffening of the depleted lithospheric mantle (DLM), caused by loss of water upon melting, could hinder mantle processing (Korenaga, 2009). Under such a mode of convection, mantle degassing becomes inefficient, and the amount of surface water could be limited over a substantial period of time.

In this article, we investigate mantle degassing during and after the solidification of a magma ocean and discuss the likelihood of ocean formation on terrestrial planets. Initial conditions necessary for planets to develop water oceans are explored for various planetary sizes and volatile compositions. Previous studies discussing the impact of mantle degassing on habitability have mostly focused on the solid-state convection stage (Noack *et al.*, 2017; Tosi *et al.*, 2017; Vilella and Kaminski, 2017; Dorn *et al.*, 2018), but the atmosphere could be dominated by volatiles degassed during the preceding magma ocean. Moreover, volatile concentrations in the mantle affect viscosity and thus the thermal evolution of planets, so it is crucial to solve for the entire history of mantle degassing self-consistently. It is noted that we assume that planets are in an oxidized condition, and the atmospheric components considered here are limited to H_2O and CO_2. The redox of the early Earth remains controversial, but recent studies suggest that planets larger than Mars would have an oxidized atmosphere (Hirschmann, 2012; Deng *et al.*, 2020).

2. Degassing During Magma Ocean: After the Final Giant Impact and Before the Solidification of the Mantle Surface

We first consider mantle degassing during the early stage of magma ocean solidification. Here the focus is on the aftermath of the magma ocean produced by late-stage giant impacts, which are common in *N*-body simulations of planetary formation (*e.g.*, Rubie *et al.*, 2015; Quintana *et al.*, 2016). The final giant impact was likely energetic enough to melt most of the mantle (Nakajima and Stevenson, 2015), so the atmosphere existing before the impact would have re-equilibrated with the magma ocean. The same is likely to be true for larger exoplanets because, with an impactor of 10% target mass, a typical impact velocity is high enough to produce substantial melting of the mantle (Stixrude, 2014). Also, the amount of radiogenic Xe in the atmosphere suggests that a catastrophic atmospheric loss likely occurred around the time of the Moon-forming giant impact (Porcelli and Pepin, 2000). Therefore, we assume that volatile partitioning would be reset by the final giant impact, and we estimate how the volatile budget would be distributed between the atmosphere and the mantle during the solidification of the final magma ocean.

The solidification of a magma ocean can be divided into two stages by its surface melt fraction (Fig. 1). With a high melt fraction at the surface, the magma ocean produces a high convective heat flux, resulting in a surface temperature high enough to maintain a molten surface (Lebrun *et al.*, 2013; Salvador *et al.*, 2017). As the mantle cools down and melt fraction becomes lower than the critical value ($\sim$0.4), however, the partially molten mantle would undergo a rheological transition and start to behave as solid (Abe, 1993b). Convective heat flux plummets and the surface temperature would drop to <500 K, which is well below the mantle solidus temperature (Lebrun *et al.*, 2013; Salvador *et al.*, 2017). Therefore, the surface layer would be completely solidified in a short timescale once the surface melt fraction reaches the critical value, even though the interior may still be partially molten. Chemical equilibrium between the mantle and the hydrosphere is not maintained thereafter, and volatile exchange between the surface and the interior would instead be characterized by solid-state convection (Abe, 1997). Although its contribution is expected to be small, some additional degassing processes may take place during the transition period from a magma ocean to solid-state convection and are discussed in Section 4.1.

In this section, we focus on volatile partitioning between the atmosphere and magma ocean while a partially molten surface is sustained, and the main goal here is to show the impact of the rheological transition on mantle degassing. We emphasize that the magma ocean considered here is produced by the final giant impact on the planet. Other degassing models have also examined the same period (*e.g.*, Elkins-Tanton, 2008; Lebrun *et al.*, 2013; Salvador *et al.*, 2017; Bower *et al.*, 2019), and ours and these studies investigate a different evolutionary stage from so-called ''accretionary magma ocean'' models (*e.g.*, Matsui and Abe, 1986; Zahnle *et al.*, 1988). The latter type of model tracks the amount of added surface water as an impactor hits the planet and considers different degassing processes from the former. Also, accretionary magma ocean models do not consider large-scale melting at the final stage of accretion, so the mantle and atmosphere are never in equilibrium in terms of volatile partitioning. We assume that a giant impact most likely induces global-scale melting (Nakajima and Stevenson, 2015), so that a substantial amount of volatiles would be partitioned into the mantle. Although both types of models aim to quantify surface water mass at the end of accretion, we caution that their validity depends on the assumed scale of mantle melting.

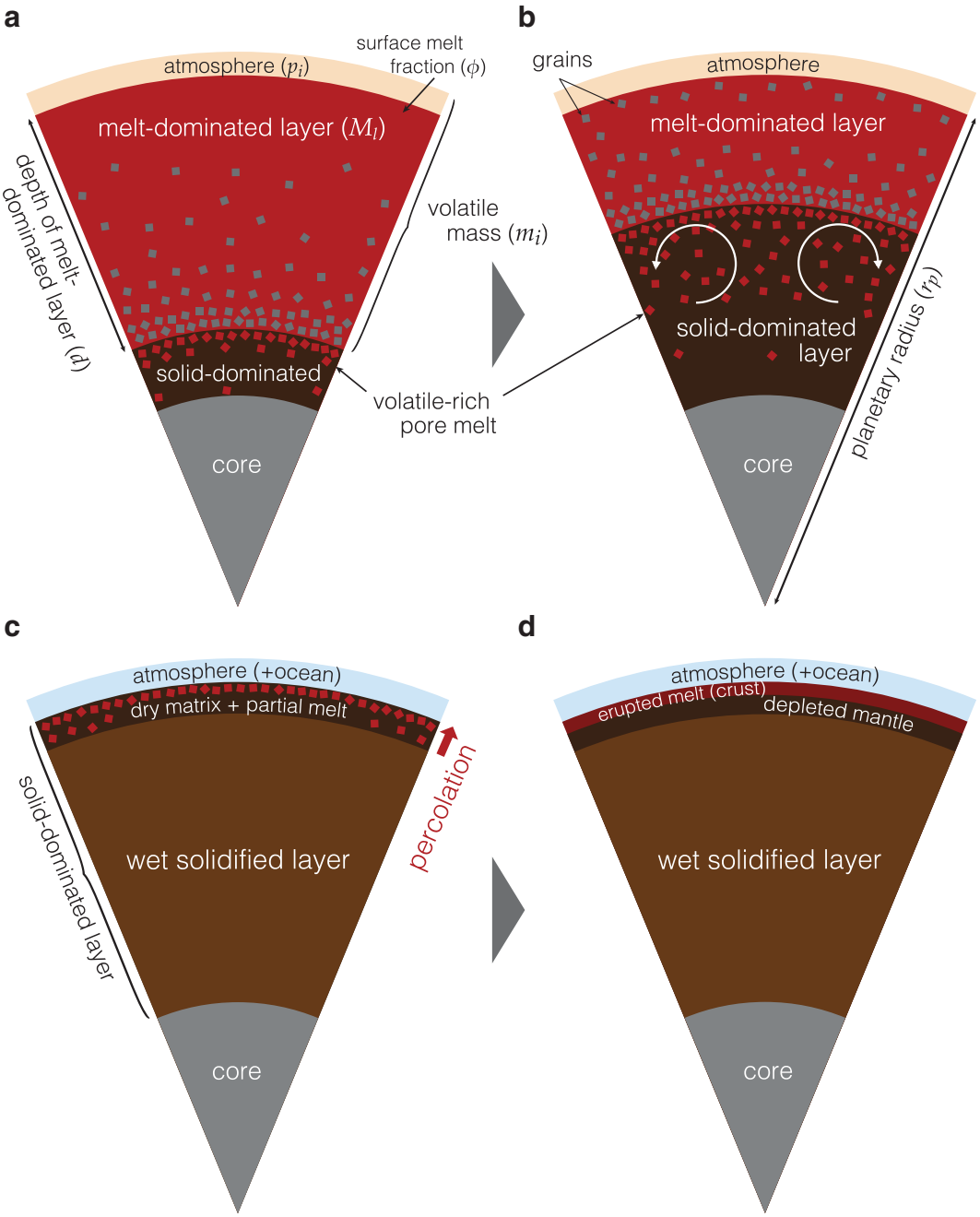

FIG. 1. Schematic illustration of the upper mantle and atmosphere during the solidification of magma ocean. **(a)** Magma ocean undergoes the rheological transition from the bottom, forming a solid-dominated layer. Melt would be trapped in pore spaces with volatiles, and thus volatiles would not concentrate in the melt-dominated layer. Variables used in Eq. 3 are labeled in the corresponding reservoirs. **(b)** Magma ocean continues to solidify, and the thickness of the solid-dominated layer grows. Rapid convection and the Rayleigh–Taylor instability would efficiently cool the melt- and solid-dominated layers, respectively, both creating an adiabatic thermal profile. Because of the rapid onset of the instability, volatiles would efficiently be sequestered in the deeper region. **(c)** When the melt-dominated layer disappears, convective heat flux plummets, and the surface temperature drops below the mantle solidus. When sufficient amount of water is degassed, oceans may form. Because melt percolation is faster than solid-state convection, percolation contributes to additional degassing. **(d)** Erupted melt forms a crust at the top, leaving a dry depleted layer below the crust. Because the deeper region is completely solidified, percolation would not occur, and most of the mantle would remain hydrated. Color graphics are available online.

2.1. Volatile partitioning

When a magma ocean behaves rheologically as liquid, the atmosphere and the magma ocean are equilibrated in a short timescale, and volatile partitioning between the magma and the atmosphere would determine the atmospheric pressure (Elkins-Tanton, 2008; Lebrun *et al.*, 2013). Magma at the surface dissolves volatiles up to their solubility limits, and volatiles in excess of saturation would reside in the atmosphere. As a magma ocean cools down, melt fraction

decreases from the lowermost part of the mantle (*e.g.*, Abe, 1993b; Solomatov, 2007), and the ''melt-dominated'' layer shrinks and the ''solid-dominated'' layer grows (Fig. 1). The two layers are separated by the rheological transition and are defined by their melt fractions as $\phi \geq 0.4$ and $\phi < 0.4$, respectively. These layers were referred to as ''soft'' and ''hard'' magma oceans in Abe (1993a). We solve for volatile partitioning and mass balance at each time step as a magma ocean undergoes the rheological transition from the bottom upward.

Volatile concentration in the surface magma, x_i, corresponds to the solubility at its atmospheric partial pressure, p_i, for each volatile species i. The solubility measurements of CO_2 and H_2O are parameterized as follows (Blank and Brooker, 1994; Lichtenberg *et al.*, 2021):

$$p_{H_2O} = \left(\frac{x_{H_2O}}{6.8\times10^{-6}}\right)^{1.42}, \quad (1)$$

$$p_{CO_2} = \left(\frac{x_{CO_2}}{4.4\times10^{-10}}\right), \quad (2)$$

where pressure is shown in the unit of Pa and concentration is shown in wt%. Some models indicate higher solubility for both H_2O and CO_2 (Papale, 1997; Gardner *et al.*, 1999), but we adopt the least soluble model to prepare the most optimistic case for ocean formation. Regardless of the model, water is predicted to be considerably more soluble in silicate melts than CO_2.

The variables p_i and x_i can be solved using the following mass balance (Bower *et al.*, 2019):

$$\phi x_i M_l + \frac{\mu_i}{\bar{\mu}}\frac{4\pi r_p^2}{g}p_i = m_i, \quad (3)$$

where ϕ is the melt fraction at the surface, M_l is the mass of the melt-dominated layer, μ_i is the molar mass of volatile i, $\bar{\mu}$ is the mean molar mass of the atmosphere, r_p is the planetary radius, and m_i is the total mass of volatile i in the atmosphere and the melt-dominated layer (Fig. 1a). The surface melt fraction ϕ is determined based on the surface temperature, T_s, and a phase diagram of peridotite (Katz *et al.*, 2003), and the surface temperature is calculated using on a one-dimensional (1D) atmospheric model of Nakajima *et al.* (1992) (see Appendices A.1 and A.2 for details).

The volatile mass m_i represents those that were not trapped in the solid-dominated layer existing in the deeper region (Fig. 1). Taking into account the rheological transition of a partially molten medium, a significant amount of melt could be trapped in the pore space of the solid matrix, together with volatiles dissolved in the melt (Fig. 1b). The percolation of pore melt is slower than the speed of magma ocean solidification (Hier-Majumder and Hirschmann, 2017), and a newly formed rheologically solid layer, which includes volatile-rich pore melt, would be quickly delivered to the deeper region by the Rayleigh–Taylor instability (Maurice *et al.*, 2017; Miyazaki and Korenaga, 2019b). The solid-dominated layer is much more viscous than the melt-dominated one, and its convection would be insignificant within the cooling timescale of the melt-dominated layer. However, because the solidus and liquidus curves of peridotite are superadiabatic (Supplementary Fig. S1), the density structure of the solid-dominated layer is gravitationally unstable after the rheological transition. With parameters estimated by Miyazaki and Korenaga (2019a, b), the entire lower mantle reaches the rheological transition in $\sim$4000 years, whereas the timescale for the Rayleigh–Taylor instability is less than a year just after the lower mantle undergoes the rheological transition. Volatiles trapped in the pore space of the solid matrix would thus be effectively sequestered in the deep mantle and be segregated from the remaining melt layer (Fig. 1a, b).

During the instability-triggered downwelling, the melt in the pore space would solidify by adiabatic compression, and the melt would be supersaturated and exsolve volatiles. Yet, the saturation limit would be reached only when melt fraction becomes lower than $\sim$0.002. Here we consider an initial H_2O content <0.1 wt%, and in such a case, concentrating volatiles by 500 times would still not result in exceeding saturation limits (Kawamoto and Holloway, 1997). Therefore, the melt–solid mixture would be mostly solidified when volatiles in melt pockets finally start to be degassed, and exsolved volatiles would either diffuse into the surrounding nominally anhydrous minerals or be trapped in the solid matrix as fluid inclusions.

Volatiles incorporated into the pore space of the solid matrix would thus be kept in the solid-dominated layer during the subsequent evolution, and we assume that the corresponding amount is subtracted from the volatile budget of the melt-dominated layer. As the magma ocean cools down and the depth of the melt-dominated layer, d, decreases, the volatile budget m_i changes as follows:

$$m_i(d-\Delta d) = m_i(d) - \phi x_i \Delta M_l, \quad (4)$$

where ΔM_l is the mass of the magma ocean that underwent the rheological transition while d decreased by Δd. Considering that vigorous convection takes place within the melt-dominated layer, the bulk volatile concentration in a crystal–melt mixture is assumed to be constant ($=\phi x_i$) throughout the melt-dominated layer. Equations 1–4 are solved until the melt-dominated layer disappears ($M_l,\ d=0$).

2.2. Degassing of the upper mantle by percolation

Once the entire mantle undergoes the rheological transition and the melt-dominated layer disappears, the evolution of a magma ocean is characterized by solid-state convection. Although percolation is slower than the Rayleigh–Taylor instability, it is faster than solid-state convection, so melt and dissolved volatiles in the pore space would escape toward the surface (Fig. 1c). Volatiles included in the partial melt would be degassed to the surface, and their amount is proportional to the mass of partially molten layer when the melt-dominated layer disappears.

We calculate its thickness from the adiabatic temperature profile with a critical melt fraction of 0.4 at the surface (Abe, 1993b; Solomatov, 2007). For simplicity, the mantle is assumed to be compositionally homogeneous and have a pyrolitic composition, and in such a case the partial melt layer would extend to a depth of $\sim$5 GPa (Appendix A.3). We note that, if the mantle experiences differentiation during magma ocean solidification, the thickness of the partial melt layer could decrease by half (Appendix A.4) (Miyazaki and Korenaga, 2022), and degassing by percolation could be smaller

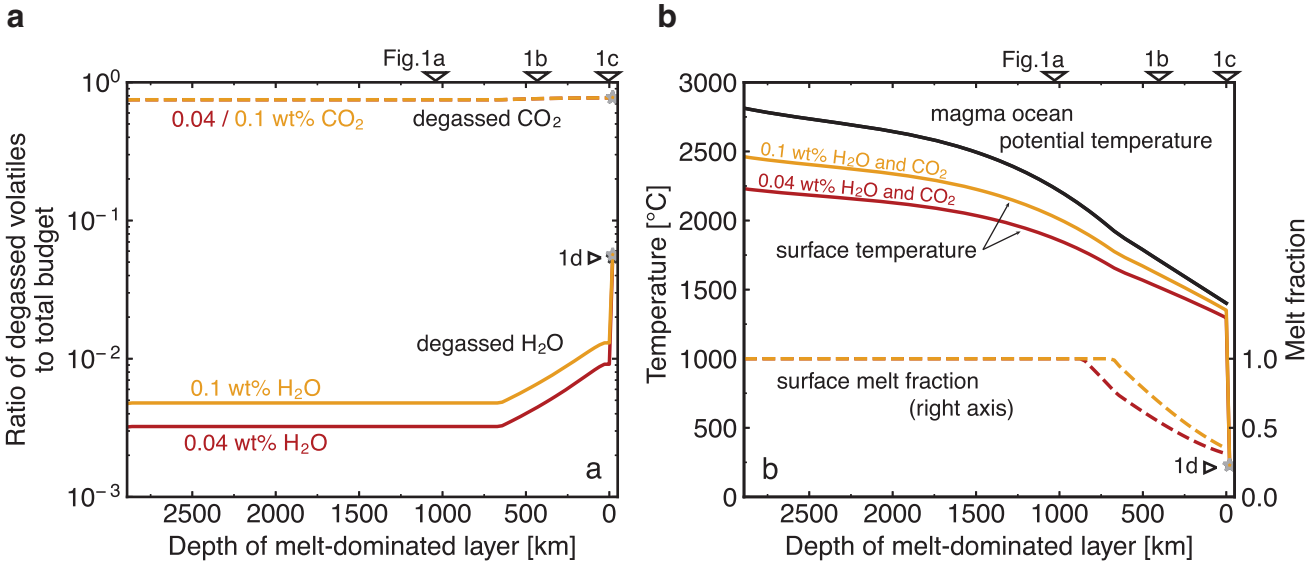

FIG. 2. The evolution of **(a)** volatiles in the atmosphere and **(b)** the thermal state as a function of the melt-dominated layer depth for an Earth-size planet. As solidification proceeds, the layer thickness decreases, so the system evolves from left to right. **(a)** The ratio of degassed volatiles to the total volatiles budget for H_2O (solid) and CO_2 (dashed). Initial mantle concentrations of 0.04 wt% (red) and 0.1 wt% (yellow) are tested for both volatiles. For H_2O, the two values correspond to 1.2 and 3 ocean masses, respectively. **(b)** The mantle potential temperature (black solid) and the surface temperature (colored solid, left axis) with the melt fraction of magma ocean at the surface (dashed, right axis). The snapshots of the mantle structure are shown in Fig. 1, with triangles indicating the corresponding panels. Color graphics are available online.

than that presented in Figs. 2–4. The mantle, however, would eventually be homogenized, and the long-term evolution of surface water would converge to results presented in Section 3.

2.3. Results

2.3.1. Degassing of Earth-size planets. Figure 2 shows a typical evolution of the atmospheric pressure for an Earth-size planet at 1 AU. A fraction of volatiles would be degassed from the beginning to maintain equilibrium with volatiles in the mantle, but further degassing is limited during the early stage of solidification because volatiles are trapped in the pore space of the solid-dominated layer, and thus volatile concentrations remain mostly unchanged (Fig. 2a). Here we assume initial volatile concentrations of 0.04 and 0.1 wt% for both H_2O and CO_2, and regardless of the initial concentration, >99% of the total H_2O budget is estimated to be retained in the mantle during the early stage of magma ocean solidification.

On the contrary, because CO_2 is less soluble to silicate magma, ~70% of the total CO_2 would be released to the atmosphere (Fig. 2a) (Hier-Majumder and Hirschmann, 2017), and such an atmosphere dominated by CO_2 would further suppress the degassing of lighter gases, including H_2O (Bower *et al.*, 2019). Degassing resumes when the surface magma starts to solidify as volatiles concentrate in the remaining melt phase (Fig. 2b), and a higher atmospheric pressure is required to maintain equilibrium between the atmosphere and the magma ocean. Degassing by percolation would also increase the volatile mass in the atmosphere, yet ~95% of H_2O would still be retained in the mantle.

2.3.2. Degassing of super-Earths. We repeat calculations in Section 2.3.1 for a range of initial volatile content and planetary mass. As expected, the pressure of degassed atmosphere increases with higher initial volatile concentrations, but a larger planetary mass does not necessarily result in a thicker atmosphere; the partial pressure for degassed H_2O atmosphere, p_{H_2O}, shows little dependence on planetary mass (Fig. 3a). This is because the majority of H_2O is stored in the mantle, and the water concentration in the mantle changes little from the initial value. Therefore, the corresponding atmospheric pressure in equilibrium with the mantle reservoir is mostly the same regardless of planetary mass. In contrast, most of the CO_2 inventory is degassed to the atmosphere, and thus p_{CO_2} becomes higher for larger planets (Fig. 3b).

The partial pressure is related to the mass of volatile i in the atmosphere, M_i, through

$$p_i = \frac{M_i g}{4\pi r_p^2}\frac{\bar{\mu}}{\mu_i} \propto M_i, \tag{5}$$

where g is the gravitational acceleration and r_p is the planetary radius. The relation between g and r_p is calculated from the simplified interior model of Seager *et al.* (2007). Therefore, with the same volatile concentrations, M_{CO_2} increases with planetary mass (Fig. 3b), whereas M_{H_2O} remains the same for planets of any size (Fig. 3a).

When the amount of surface H_2O is small, the entire surface water budget can exist as vapor in the atmosphere without forming water oceans. The threshold amount of H_2O for ocean formation is estimated using a 1D radiative-convective model of Nakajima *et al.* (1992). The model predicts that the threshold amount increases with a thicker

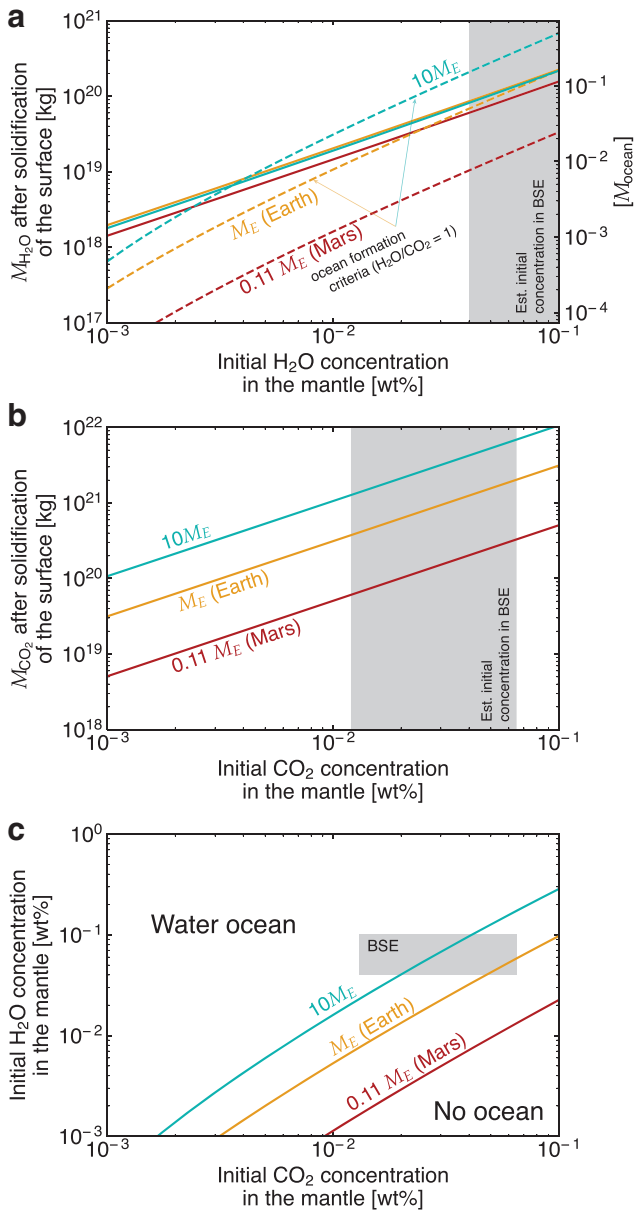

FIG. 3. **(a, b)** Atmospheric mass of **(a)** H_2O and **(b)** CO_2 when the surface of the magma ocean solidified, as a function of the initial volatile concentration. Colors denote different planetary sizes: Mars- (red), Earth-size (M_E, yellow), and $10M_E$ super-Earths (cyan). The value of M_{H_2O} is similar among planets of different sizes, and all lines are very close to each other. In **(a)**, the minimum amount of H_2O necessary to stabilize water oceans is also plotted, assuming that the H_2O/CO_2 mass ratio is 1. Mars- and Earth-size planets would have sufficient amount of water to form oceans, whereas $10M_E$ super-Earths would lack oceans immediately after the solidification of the mantle surface. **(c)** Conditions necessary for water ocean formation as a function of initial H_2O and CO_2 concentrations. Colored lines separate the two regimes: the formation (upper left) and absence of water oceans (lower right) when the mantle surface solidified. With the same volatile concentrations, smaller planets are more likely to develop water oceans. Shaded rectangles represent the estimated volatile concentrations in the BSE from Hirschmann and Dasgupta (2009) and Korenaga *et al.* (2017). BSE, bulk silicate Earth. Color graphics are available online.

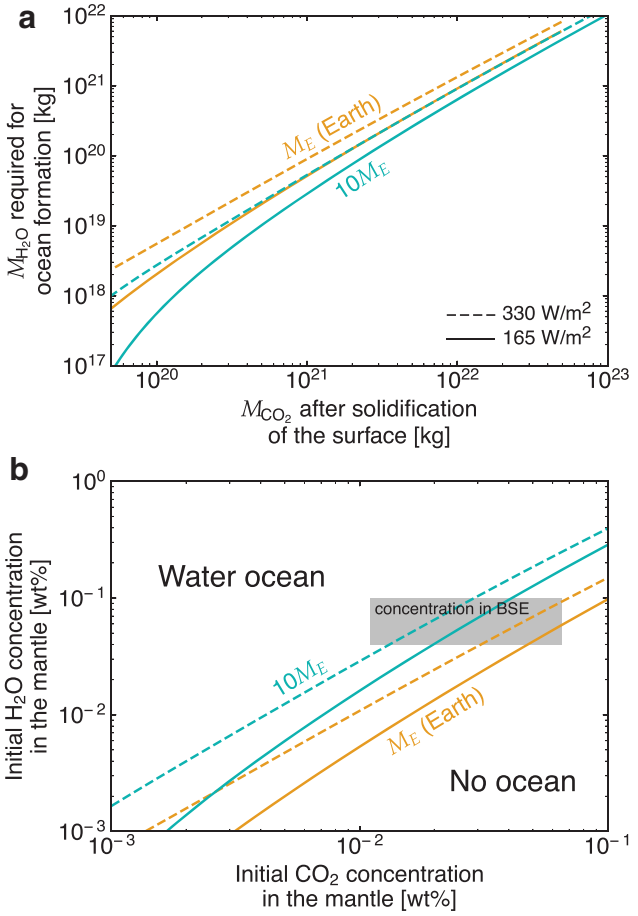

FIG. 4. **(a)** The minimum amount of surface H_2O required to form water oceans as a function of M_{CO_2}. Results are calculated for different levels of net stellar radiation: 165 (solid, early Earth) and 330 W m^{-2} (dashed, early Venus). Colors denote different planetary sizes: Earth-size (M_E, yellow) and 10 M_E super-Earth (cyan). **(b)** The same as Fig. 3c but with different levels of net stellar radiation. Colored lines separate the two regimes: the formation (upper left) and absence of water oceans (lower right) when the planetary surface solidified. Planets further away from the central star are more likely to develop water oceans, but planetary size plays a larger role in characterizing ocean formation. Shaded rectangles represent the estimated volatile concentrations in the BSE from Hirschmann and Dasgupta (2009) and Korenaga *et al.* (2017). Color graphics are available online.

CO_2 atmosphere (Abe, 1993a; Salvador *et al.* 2017) because a thicker atmosphere can contain more H_2O vapor, and its amount further increases under a higher surface temperature induced by a stronger greenhouse effect. Under the same initial volatile concentrations, therefore, larger planets are less likely to develop water oceans immediately after the solidification of the mantle surface (Fig. 3a, c). For an initial CO_2 concentration of 0.01 wt%, the amount of degassed CO_2 (M_{CO_2}) increases from 5.1×10^{19} kg for a Mars-size planet to 1.1×10^{21} kg for a $10M_E$ super-Earth (Fig. 3b), which would raise the amount of surface H_2O required to develop water oceans from $\sim1.6\times10^{18}$ kg to $\sim3.1\times10^{19}$ kg (Fig. 3a).

Nevertheless, the amount of surface water M_{H_2O} does not change with planetary size, where M_{H_2O} is $\sim 2 \times 10^{19}$ kg for any planets with an initial H_2O concentration of 0.01 wt%. Smaller planets are thus more likely to develop water oceans when the surface of the mantle solidifies. How the initial volatile concentration of terrestrial planets is characterized is still debated (Hirschmann *et al.*, 2021; Li *et al.*, 2021), but if terrestrial exoplanets have similar volatile concentrations to Earth, super-Earths may lack water oceans when the surface of the mantle solidifies (Fig. 3c).

It is noted that the minimum surface H_2O mass to form water oceans in Fig. 3a is associated with an uncertainty of a factor of ~ 2 because a 1D gray atmospheric model is adopted here. Considering that the subsiding branch of the atmospheric circulation is undersaturated with water vapor, the average relative humidity should be <1 (*e.g.*, Ishiwatari *et al.*, 2002; Abe *et al.*, 2011; Pierrehumbert and Ding, 2016). It is thus assumed that the relative humidity is 0.7 throughout the troposphere in our model, but this value remains unconstrained for an atmosphere with an extreme CO_2 concentration and may range between 0.5 and 1. Also, CO_2 existing near the surface could be in a supercritical state when p_{CO_2} is >74 bar. Although the temperature and pressure conditions considered here are distant from its critical point, physical properties including opacity may differ by some degree from the gas state. Implementing these factors, together with the wavelength dependence of the opacity, may modify our estimate of the minimum H_2O mass required for ocean formation by some factor. The overall trend of our results is unlikely to change, but a more detailed model would be needed to predict the actual threshold.

2.4. Discussion: early Earth and early Venus

The amount of volatiles in the bulk silicate Earth (BSE) could have been just above the threshold for stabilizing water oceans at the point of magma ocean solidification. Although the volatile content in the terrestrial mantle remains controversial, recent estimates suggest that the mantle and the hydrosphere in total contain 1.2–3 ocean mass of H_2O (Hirschmann and Dasgupta, 2009; Korenaga *et al.*, 2017) and $4.8–26 \times 10^{20}$ kg of CO_2, which translates to initial concentrations of 0.04–0.1 wt% and 0.01–0.07 wt%, respectively, when all volatiles are dissolved in the mantle. The estimated volatile concentrations lie just inside the boundary between the regimes of ocean formation and dry surface (Fig. 3c), and if BSE had a lower bound H_2O and an upper bound CO_2 concentration, water oceans may have been absent during the early stage of evolution.

As we discuss in Section 3, the rate of mantle degassing decreases substantially after the mantle surface solidifies, and thus the surface would continue to lack water oceans if oceans are absent at the time of surface solidification. The presence of surface water in the Hadean has been suggested from zircon records (*e.g.*, Mojzsis *et al.*, 2001; Wilde *et al.*, 2001), so water oceans were likely present on the surface of Earth from the beginning of its evolution. A combination of a low H_2O and a high CO_2 concentration in BSE (>0.05 wt%) may be ruled out if water oceans indeed existed on the surface of the Hadean Earth.

The early Venus, on the contrary, may have lacked water oceans because a larger amount of surface H_2O is required for planets closer to the central star (Fig. 4a). Assuming the same albedo, the net solar radiation for the early Venus was 330 W m^{-2}, which is two times higher than the value for the early Earth. To balance stronger solar radiation, the overall thermal structure, including the planetary surface, becomes hotter, thus allowing more H_2O to exist as water vapor in the atmosphere (Nakajima *et al.*, 1992). The minimum amount of H_2O to form oceans doubles for a M_{CO_2} of 10^{21} kg and increases by a factor of 5 for $M_{CO_2} \sim 10^{20}$ kg. As a result, for a planet receiving 330 W m^{-2} of stellar radiation, water oceans would be absent for a wider range of initial volatile concentrations.

If Venus had similar volatile concentrations to Earth, our result suggests that Venus would develop water oceans only for a combination of a high H_2O and a low CO_2 concentration (Fig. 4b). Because the threshold for ocean formation lies within the estimated volatile concentrations in BSE, the location of planets and thus the amount of net solar radiation may have decided the fate of two similar planets (see Section 3.3 for further discussions). Mars, on the contrary, likely developed water oceans immediately after magma ocean solidification because of its small size (Fig. 3c) and its distance from the Sun.

Volatile concentration required to develop water oceans is much higher in our model than that estimated in Salvador *et al.* (2017) because we take into account volatiles that are trapped in the pore space of the melt–solid mixture. Models of magma ocean solidification have often neglected this effect and assumed that volatiles, behaving as incompatible elements, concentrate in the residual melt layer as the magma ocean solidifies from the bottom to the top (Elkins-Tanton, 2008; Hamano *et al.*, 2013; Lebrun *et al.*, 2013; Salvador *et al.*, 2017). In such a scenario, the concentration of volatiles eventually exceeds saturation levels and results in efficient degassing. Volatiles, however, would not be efficiently degassed because the compaction of melt–solid mixture is slow (Hier-Majumder and Hirschmann, 2017) and because the Rayleigh–Taylor instability efficiently delivers volatile-rich pore melt to the deeper mantle. Therefore, the remaining melt layer near the surface experiences little change in volatile concentrations, and the mantle is likely to remain hydrated (Section 2.1, Fig. 2a).

3. Degassing During Solid-State Convection: After the Solidification of the Mantle Surface

Once the surface of the mantle solidifies, mantle degassing during the subsequent evolution would be characterized by solid-state convection. Although partial melt may still exist in the interior, the planetary surface would be covered by a solidified lid, and the mode of volatile exchange would be similar to what is seen on the present-day Venus and Mars (Noack *et al.*, 2017; Dorn *et al.*, 2018). The solid lid prohibits the mantle and the hydrosphere to reach equilibrium, and instead the evolution of the atmosphere becomes controlled by a balance between ingassing to and degassing from the mantle. The rate of ingassing and degassing differs appreciably depending on the mode of solid-state convection, so whether the mantle operates under plate tectonics or stagnant lid convection would control the atmospheric evolution of terrestrial planets. Here, plate tectonics refers

to a mode that allows the continuous recycling of the uppermost layer, whereas in stagnant lid convection a rigid immobile shell covers the surface, and convective motion is limited to the interior region beneath the shell (Solomatov, 1995).

The key to triggering plate tectonics is the weakening of oceanic lithosphere (Moresi and Solomatov, 1998), and several mechanisms have been proposed, including grain-size reduction (*e.g.*, Kameyama *et al.*, 1997; Bercovici and Ricard, 2012) and thermal cracking (Korenaga, 2007). Comparison between different mechanisms is discussed in several reviews (Bercovici *et al.*, 2015; Korenaga, 2020), but the weakening of the strongest part of the lithosphere requires the reduction of friction coefficient by some means, for which thermal cracking is so far the only mechanism that is consistent with our understanding of rock mechanics. Positive feedback between thermal cracking and serpentinization could potentially hydrate the lithosphere deeply (Korenaga, 2017), with trapped water reducing lithostatic-hydrostatic pressure difference and thus effective friction coefficient.

The presence of surface water is likely the key to lowering the yield strength of the lithosphere, and although the mechanism is different, the importance of surface water in triggering plate tectonics has been suggested in other studies as well (Regenauer-Lieb *et al.*, 2001; Gerya *et al.*, 2008). Indeed, other oceanless planets, including Venus, Mars, and Moon, are generally considered to be operating under the mode of stagnant lid convection. Sporadic subduction may be triggered by large meteorite impacts during the early stage of planetary evolution (Hansen, 2007; O'Neill *et al.*, 2017), but its effect is likely to be ephemeral, and the mode of convection would revert to stagnant lid without water oceans.

The absence of surface water thus leads to stagnant lid convection, which limits both ingassing and outgassing compared with plate tectonics (Kite *et al.*, 2009). Under solid-state convection, the degassing of the mantle is triggered when the mantle material undergoes partial melting during its upwelling (Fraeman and Korenaga, 2010; O'Rourke and Korenaga, 2012), but a rigid immobile shell would limit the extent of such upwelling motion. With the same convective velocity, the processing of the mantle would be significantly slower for stagnant lid convection than plate tectonics, under which the mantle material is brought up all the way to the surface. Oceanless planets would therefore have a smaller supply of H_2O from the mantle than those with oceans, implying that an oceanless state may persist for the geological time.

The lack of surface recycling also prevents the transport of volatiles from the hydrosphere to the mantle, whereas the sequestration of volatiles is possible under plate tectonics (Sleep and Zahnle, 2001; Miyazaki and Korenaga, 2022). Volatiles, in particular CO_2, can be stored in oceanic crust as carbonate minerals (*e.g.*, Alt and Teagle, 1999), which could then be delivered to the interior by subduction. The majority of atmospheric CO_2 existed after magma ocean solidification on Earth should have been transported to the mantle by the end of Hadean (Catling and Zahnle, 2020), and a rapid removal of atmospheric CO_2 is also expected for other terrestrial planets with plate tectonics. On the contrary, the removal of atmospheric CO_2 would be inhibited for stagnant lid convection, and CO_2 would continue to accumulate in the atmosphere by mantle degassing. The threshold amount of H_2O to develop water oceans thus continues to increase with time for such planets, which would be another factor that further delays the formation of water oceans.

Here, we estimate how long it takes for initially oceanless dry planets to develop water oceans after solid-state convection starts, by modeling the thermal evolution of terrestrial planets. Previous studies discussing habitability in the context of stagnant lid convection have focused on the degassing of CO_2 because the availability of greenhouse gas on the surface was considered to regulate the outer edge of the habitable zone (Noack *et al.*, 2017; Tosi *et al.*, 2017; Vilella and Kaminski, 2017; Dorn *et al.*, 2018). However, they have not taken into account the massive CO_2 atmosphere released during magma ocean (Fig. 2a), and with its effect included, the amount of greenhouse effect should not be a limiting factor for habitability for planets with stagnant lid convection. Because the focus of this article is the formation of water oceans on terrestrial planets, we do not model the evolution after water oceans form, but its impact on habitability is discussed in Section 4.2.

3.1. Methods: mantle degassing under stagnant lid convection

The degassing rate of terrestrial planets that initially lack water oceans is calculated based on a heat flow scaling of stagnant lid convection (Korenaga, 2009). This scaling has been applied to the evolution of Mars, Venus, and super-Venus planets (Fraeman and Korenaga, 2010; O'Rourke and Korenaga, 2012), where they modeled the thermal evolution of crust, mantle, and core self-consistently by incorporating the influence of mantle processing on rheology and radiogenic heating. Our theoretical formulation follows Fraeman and Korenaga (2010) and O'Rourke and Korenaga (2012), and readers are referred to these studies for details. We summarize the key equations of our model in the following, focusing on the difference from previous models.

Our primary goal is to estimate the processing rate of the mantle to track the atmospheric evolution over time: melting by adiabatic decompression generates new crust and DLM, and volatiles are degassed during crust formation. A wide range of initial conditions were explored in O'Rourke and Korenaga (2012), but subsolidus convection likely starts immediately after the surface of the mantle solidifies and degassing by percolation takes place (Section 2.2). We thus adopt the thermal structure and volatile concentrations predicted in Section 2 as initial conditions to model the history of mantle degassing in a self-consistent manner.

3.1.1. Scaling of stagnant lid convection. The vigor of convection is characterized by the Nusselt number: convective heat flux normalized by conductive heat flux. The Nusselt number, Nu, is calculated through a local stability analysis of the top thermal boundary layer (TBL) (Korenaga, 2009), and we consider a condition where a bottom fraction of the boundary layer becomes gravitationally unstable. The Nusselt number is a function of the following variables: the mantle potential temperature, T_m; the temperature difference across the TBL, ΔT; the mantle viscosity at the base of the TBL, η_m; viscosity increase by

dehydration, $\Delta\eta_w$; and the thickness of the DLM, h_{DLM}. The temperatures T_m and ΔT are solved from the energy balance of the mantle, and η_m is calculated as a function of potential temperature T_m and volatile concentrations in the mantle (Section 3.1.2). The evolution of h_{DLM} is controlled by the combination of mantle processing, delamination, and rewetting (Section 3.1.3).

DLM lacks volatiles, so the layer is more viscous than the source mantle. Thermal convection is suppressed with such effect of dehydration stiffening (van Thienen, 2007), and its effect is stronger for a higher mantle potential temperature because of a thicker DLM. For a potential temperature of 1600°C, the TBL becomes thicker by a factor of $\sim$5 than what is predicted in a scaling without dehydration (Korenaga, 2009). Therefore, hotter mantle does not indicate more efficient thermal convection, and considering the effect of dehydration stiffening is crucial for estimating *Nu*. The thickness of the TBL can be calculated as $h_{\mathrm{TBL}} = h_{\mathrm{cm}}/Nu$, where h_{cm} is the depth of the convective mantle.

3.1.2. Mantle rheology. Viscosity η_m is described as a function of mantle potential temperature T_m and water content, c_w:

$$\eta_m = \begin{cases} A\exp\left(-\dfrac{E}{RT_m}\right)(\Delta\eta_w)^{1-c_w/c_0} & (c_w \le c_0), \\ A\exp\left(-\dfrac{E}{RT_m}\right)\left(\dfrac{c_0}{c_w}\right) & (c_w > c_0), \end{cases} \tag{6}$$

where E is an activation energy (300 kJ mol^{-1}) and R is the universal gas constant. Viscosity is assumed to decrease linearly with the water concentration c_w (Jain *et al.*, 2019; Mei and Kohlstedt, 2000), but an exponential relation is adopted below a cutoff value, $c_0 = 50$ ppm, to prevent viscosity from reaching infinity. CO_2 might also reduce mantle viscosity, but because it is mostly degassed before the solidification of the mantle surface (Fig. 2a), its effect is not considered.

Viscosity contrast between dry and wet mantle of $c_w = c_0$ is assumed to be $\Delta\eta_w = 125$ (Hirth and Kohlstedt, 1996; Mei and Kohlstedt, 2000), and we adjust the pre-exponential constant, A, so that viscosity is 10^{19} Pa s at 1350°C and $c_w = 0.04$ wt% as suggested from rock mechanics and the possibility of small-scale convection beneath oceanic lithosphere (Davaille and Jaupart, 1994; Dumoulin *et al.*, 1999; Hirth and Kohlstedt, 1996). Initial volatile concentrations in the mantle are chosen from Figs. 3c and 4b, so that water oceans are absent at the beginning of solid-state convection stage.

3.1.3. Mantle processing and crust formation. The processing of the mantle is assumed to start at a depth where the temperature exceeds a dry solidus. A wet mantle has a lower solidus temperature (*e.g.*, Kawamoto and Holloway, 1997), but the mantle would not be completely dehydrated until the melt fraction becomes sufficiently large, which becomes possible after crossing the dry solidus (*e.g.*, Hirth and Kohlstedt, 1996). The initial depth of mantle processing can thus be approximated by the dry solidus, and we parameterize the initial pressure of melting, P_i [GPa], as

$$P_i = \frac{T_m - 1423\ \mathrm{K}}{100}. \tag{7}$$

The melting is assumed to stop where it reaches the base of the TBL at $P_f = \rho_L g(h_{\mathrm{TBL}} + h_c)$, where ρ_L is the lithosphere density and h_c is the crustal thickness. The thickness of melting zone, h_p, can be described as

$$h_p = \frac{P_i - P_f}{\rho_L g}, \tag{8}$$

and assuming that downwelling is much more localized than upwelling, the volumetric rate of mantle processing is given by

$$\dot{V}_{\mathrm{proc}} = \frac{2h_p u_{\mathrm{conv}}}{h_{cm}} 4\pi r_p^2. \tag{9}$$

We adopt the scaling of Solomatov and Moresi (2000) for the average convective velocity beneath the stagnant lid:

$$u_{\mathrm{conv}} = 0.38\frac{\kappa}{h_{cm}}\left(\frac{Ra}{\theta}\right)^{\frac{1}{2}}, \tag{10}$$

where κ is the thermal diffusivity, Ra is the internal Rayleigh number, and θ is the Frank–Kamenetskii parameter. Convective velocity is influenced by the viscosity contrast across the stagnant lid and thus is a function of θ, which describes the degree of temperature dependency of viscosity:

$$\theta = \frac{E\Delta T}{RT_m^2}. \tag{11}$$

With a typical activation energy of $E = 300$ kJ mol^{-1} (Section 3.1.2), θ is $\sim$14 at a mantle temperature of 1600°C, corresponding to a state immediately after magma ocean solidification.

Finally, we can calculate the volumetric melt productivity by multiplying $\dot{V}_{\mathrm{proc}}$ by the average melt fraction in the partial melt layer, $\bar{\phi}$, which is estimated based on the melt productivity by adiabatic decompression ($d\phi/dP = 0.1$ GPa^{-1}). The growth of crust is equivalent to the volumetric melt productivity, and the volume of DLM increases by

$$\dot{V}_{\mathrm{DLM}} = \left(1 - \bar{\phi}\right)\dot{V}_{\mathrm{proc}}. \tag{12}$$

Volatiles included in the processed mantle are released to the mantle, and the rate of degassing is proportional to $\dot{V}_{\mathrm{proc}}$ as well. Volatiles are highly incompatible at the depths where melting occurs, so we consider that the processed mantle becomes entirely dry after melting. It is noted that, in some previous studies, some large fraction of volatiles (90% of volatiles with 10% melting) was assumed to remain in the depleted mantle after melting (Noack *et al.*, 2017; Dorn *et al.*, 2018), which could underestimate the efficiency of degassing a factor of $\sim$10.

Crustal thickness continues to grow by mantle processing, but the thickness of the DLM can be reduced by delamination or rehydration from the underlying mantle. When the TBL is thinner than DLM ($h_{\mathrm{DLM}} > h_{\mathrm{TBL}}$), DLM would be eroded by convection (Fig. 5), so we assume that such a delaminated fraction of DLM becomes mixed with the source mantle. Volatile concentrations in the mantle would be diluted as a result of mixing, and we adjust the concentrations accordingly (Fraeman and Korenaga, 2010). Also, DLM is continuously rewetted by hydrogen diffusion from

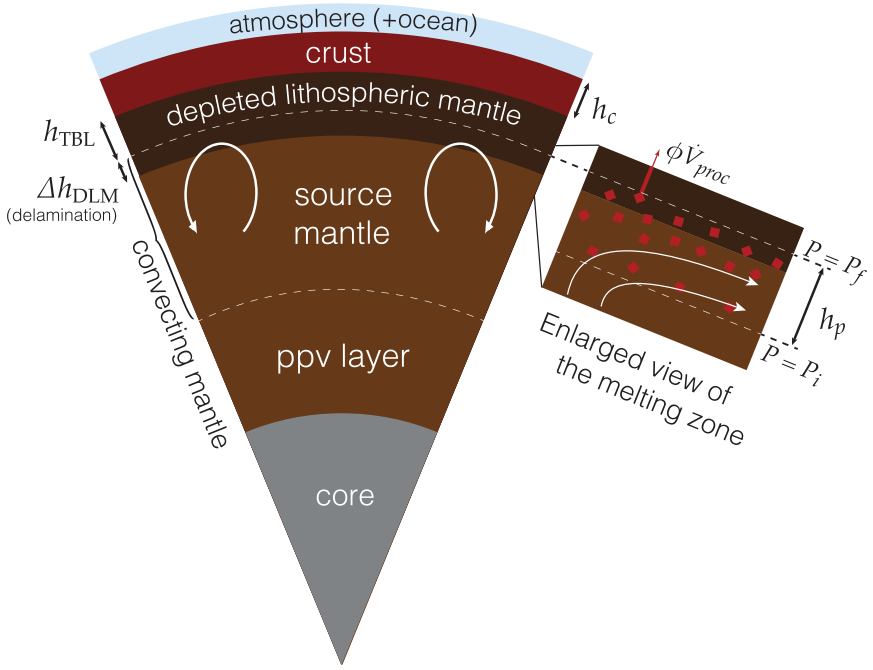

FIG. 5. Schematic illustration of the structure of terrestrial planets, and parameters described in Section 3.1 are labeled. When the DLM layer is thicker than the TBL, the excess layer would delaminate and be mixed with the source mantle. The values of $h_{\rm DML}$ shown in the subsequent figures are those after delamination. An enlarged view of the melting zone is also shown as an inset on the right. DLM, depleted lithospheric mantle; TBL, thermal boundary layer. Color graphics are available online.

the underlying mantle. At each time step, a diffusion length $\Delta h_{\rm DLM} = \sqrt{D_{\rm diff}\Delta t}$ is calculated, and we assume that the lower $\Delta h_{\rm DLM}$ of DLM is reincorporated into the source mantle reservoir. The diffusion coefficient is taken from a parameterization given in Korenaga (2009):

$$D_{\rm diff} = 6\times 10^{-5}\ {\rm m^2 s^{-1}} \times \left(-0.0027 + 2.19\times 10^{-6}(T_m - 273)\right). \quad (13)$$

Diffusive rewetting is not considered when DLM thickness is reduced by delamination.

The initial thicknesses of crust (h_c) and DLM ($h_{\rm DLM}$) are inherited from the last stage of magma ocean solidification. As discussed in Section 2.2, the uppermost partially molten layer becomes depleted in volatiles through melt escape by percolation when the surface of the mantle solidifies (Fig. 1d). The bottom pressure of the initially processed mantle is set to $\sim$5 GPa, which is equivalent to $\sim$170 km for Earth-size planets and $\sim$80 km for $5M_E$ super-Earths.

3.1.4. Thermal evolution of the mantle. The thermal evolution of the convecting mantle is controlled by a balance of radiogenic heating, heating from the core, convective heat flux of the mantle, and latent heat of mantle melting:

$$\rho_m C_m V_{cm} \gamma_m \frac{dT_m}{dt} = \frac{4}{3}\pi\left(r_m^3 - r_c^3\right)Q_m + 4\pi\left(r_c^2 F_c - r_m^2 F_m\right) - \rho_L f_m L_m, \quad (14)$$

where ρ_m is the average density of mantle, C_m is the specific heat of mantle, V_{cm} is the volume of convective mantle, r_m and r_c are the radii of the mantle and core, Q_m is the radiogenic heat production per unit volume, and L_m is the latent heat of mantle melting per unit mass. The constant γ_m is adopted to convert potential temperature to the average temperature of the mantle. The convective heat flux of the mantle, F_m, can be calculated from Nu (Section 3.1.1), and heat flux from the core, F_c, is derived using the scaling of Stevenson *et al.* (1983).

The convecting mantle represents the whole mantle for planets smaller than Earth size, but the deeper region of super-Earths may be too viscous for convection because its major constituting mineral, postperovskite, is expected to have viscosity higher by a few orders of magnitude than the terrestrial mantle (Tackley *et al.*, 2013). We thus assume that only the region shallower than $P_{ppv} =$ 200 GPa participates in thermal convection, and the value of V_{cm} is adjusted accordingly.

Also, heat flux supplied to the convecting mantle would be limited to those from radiogenic decay because an extreme viscosity suppresses the cooling of the deeper mantle (Tackley *et al.*, 2013; Dorn *et al.*, 2018) and the core. With a postperovskite viscosity of 10^{24} Pa s, which is $\sim 10^5$ higher than that of the typical upper mantle, a local stability analysis of the bottom boundary layer (Stevenson *et al.*, 1983) suggests that core cooling would be smaller by a factor of $\sim$50 for super-Earths. The presence of postperovskite should thus lead to the efficient cooling of the shallower mantle while maintaining a hot deep interior, and such an effect is incorporated into our parameterized convection model.

3.2. Results

3.2.1. Evolution of Earth-size planets. Figure 6 shows the thermal evolution and degassing history of a typical

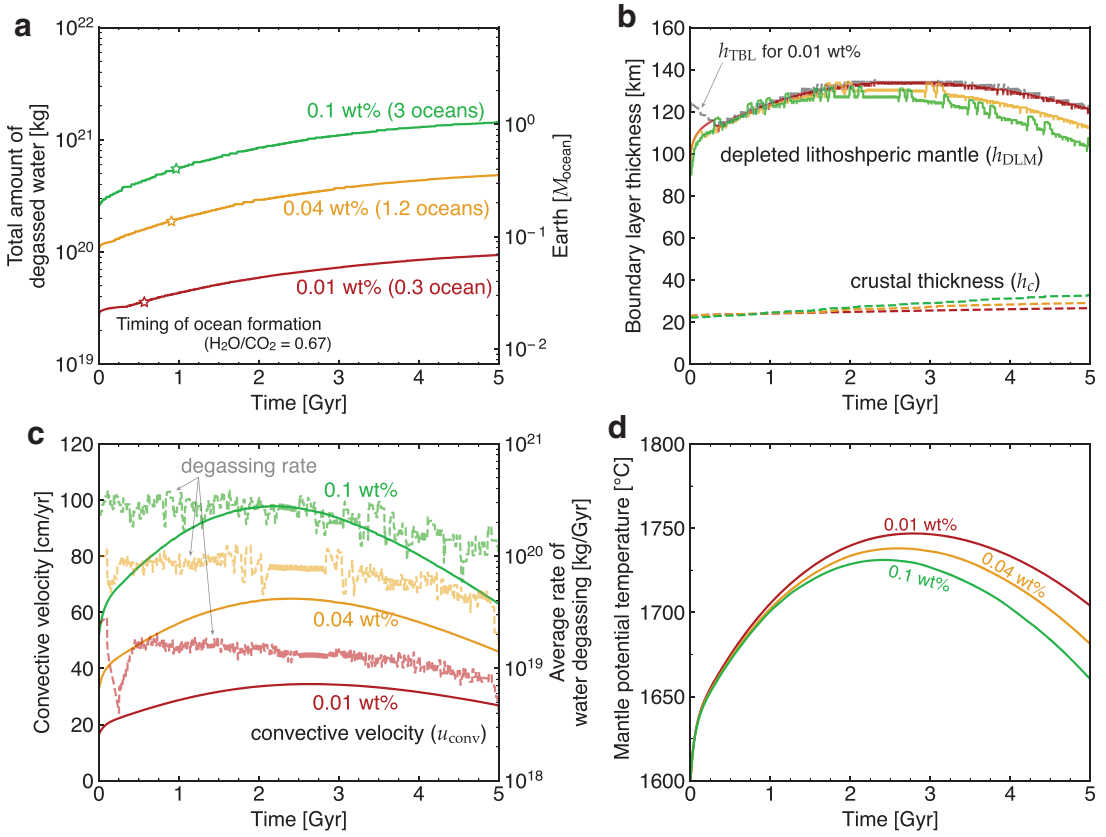

FIG. 6. The thermal evolution and degassing history of Earth-size planets under stagnant lid convection. **(a)** Total amount of degassed water, **(b)** thicknesses of crust (dashed) and DLM (solid), **(c)** convective velocity beneath the lid (solid) and the rate of water degassing averaged over 50 Myr (dashed, light colored), and **(d)** mantle potential temperature are shown for three different initial H_2O concentrations: 0.01 (red), 0.04 (yellow), and 0.1 wt% (green), corresponding to a total H_2O mass of 0.3, 1.2, and 3 ocean masses, respectively. Initial conditions are adopted from the final results of the magma ocean degassing model described in Section 2. Markers in (a) show the time when a threshold amount of surface H_2O is degassed to stabilize water oceans. The H_2O/CO_2 ratios of 0.66 (star) and net stellar radiation of 330 W m^{-2} are adopted here. With an H_2O concentration of 0.04 wt%, p_{CO_2} corresponds to $\sim$330 bar. Once water oceans form at the surface, the mode of convection likely changes to plate tectonics, so modeling results after ocean formation would underestimate convective heat flux and the rate of mantle degassing. The gray line in (b) describes the thickness of TBL. As a result of convective delamination, h_{DLM} becomes almost identical to h_{TBL} throughout the planetary evolution. Color graphics are available online.

Earth-size planet, which illustrates that mantle degassing continues but gradually decreases throughout its evolution (Fig. 6a). The rate of mantle degassing can be understood from change in the thickness of DLM (h_{DLM}) because mantle processing is reflected in the growth of DLM. During the first $\sim$2 Gyr, the depth where mantle melting starts becomes deeper with time (Fig. 6b) as mantle temperature increases by radioactive elements. Therefore, the net growth of DLM is observed, resulting in efficient degassing during this period (Fig. 6c). In the subsequent stage, however, mantle temperature decreases with time, and the mantle is newly processed only as DLM delaminates or is rewetted by hydrogen diffusion.

The growth of DLM by mantle melting and its delamination by convective erosion are occurring concurrently, and the two competing processes maintain h_{DLM} comparable with h_{TBL} (Fig. 6a). As a result, degassing is less efficient than in the first 2 Gyr even though the temperature is higher, and its rate further slows down as the mantle cools down and convective velocity decreases (Fig. 6c, d). It is noted that the rate of degassing experiences temporal fluctuation as a result of convective delamination. The bottom part of DLM becomes unstable when a sufficient fraction of DLM is rewetted by hydrogen diffusion. The resulting delamination of DLM allows mantle upwelling to reach a shallower depth, briefly triggering a larger degree of new melting.

We ran the model for different initial water concentrations, and the results show that, under the same H_2O/CO_2 ratio, the timing of water ocean formation depends weakly on the H_2O content (x_{H_2O}; Fig. 6a). This is a result of two competing processes. Because of a lower viscosity, convective velocity and thus the rate of mantle processing are higher for a wetter mantle: a mantle with a $\times 10$ higher H_2O concentration has >10 times higher H_2O degassing rate. Yet, the amount of surface H_2O necessary to stabilize oceans also becomes increasingly larger: an order of magnitude larger CO_2 concentration would require a surface H_2O amount larger by 40 times (Fig. 3a). These two effects nearly cancel out, and thus an oceanless world persists for a similar duration as long as the H_2O/CO_2 ratio remains the same. Plate tectonics would operate once the threshold is reached (Korenaga, 2020), and mantle degassing would become

more efficient afterward. A wet surface is thus expected to be maintained during the subsequent evolution.

For an Earth-size planet, the atmosphere contains ~5% of the total H_2O budget immediately after the solidification of the mantle surface (Fig. 2a), and an additional ~6% would be degassed in the next 1 Gyr during solid-state convection (Fig. 6a). These estimates correspond to initial H_2O concentrations between 0.01 and 0.1 wt%. For an H_2O/CO_2 ratio of 0.67, ~10% of the total H_2O budget needs to reside at the surface to stabilize water oceans, and such a condition is satisfied only after 0.5–1 Gyr of evolution (Fig. 6a). Because degassing slows down with time, and a planet with a smaller H_2O/CO_2 ratio requires an increasingly longer duration to form water oceans. The H_2O/CO_2 ratio therefore largely characterizes when oceans emerge on terrestrial planets.

We note that a thick DLM acts as a limiting factor for heat transport and thus mantle degassing (Fig. 7). In a conventional scaling of stagnant lid convection, which does not consider dehydration stiffening, a higher mantle temperature leads to a thinner TBL, and thus a higher convective heat flux to promote cooling (the case of $\Delta\eta = 1$; Solomatov and Moresi, 2000). Assuming such a scaling, the mantle is predicted to be efficiently processed from the beginning, crustal thickness would rapidly grow (Fig. 7b), and water oceans would form within the first 100 Myr (Fig. 7a). Neglecting dehydration stiffening thus severely overestimates the rate of mantle degassing. In reality, the presence of a dry DLM impedes convection, and the TBL becomes thicker at higher mantle potential temperatures (Fig. 6a, c).

The Nusselt number Nu is inversely proportional to h_{TBL}, so a hotter mantle actually results in lower convective heat flux (Korenaga, 2009). Because of inefficient cooling, excess radiogenic heat production heats up the mantle during the first ~1.5 Gyr (Fig. 6c), and mantle temperature starts to decrease only after this period. The depth where mantle melting starts then becomes shallower with time, DLM thins, and with a weaker influence of dehydration stiffening, h_{TBL} starts to decrease (Fig. 6a). A larger viscosity contrast between dry and wet mantle $\Delta\eta_w$ further delays the rate of cooling and degassing, and thus better constraining the dependence of viscosity on water content would be important to accurately predict the timing of ocean formation. Some experimental studies suggest that the water dependence of mantle viscosity can be more drastic than that assumed here (Faul and Jackson, 2007).

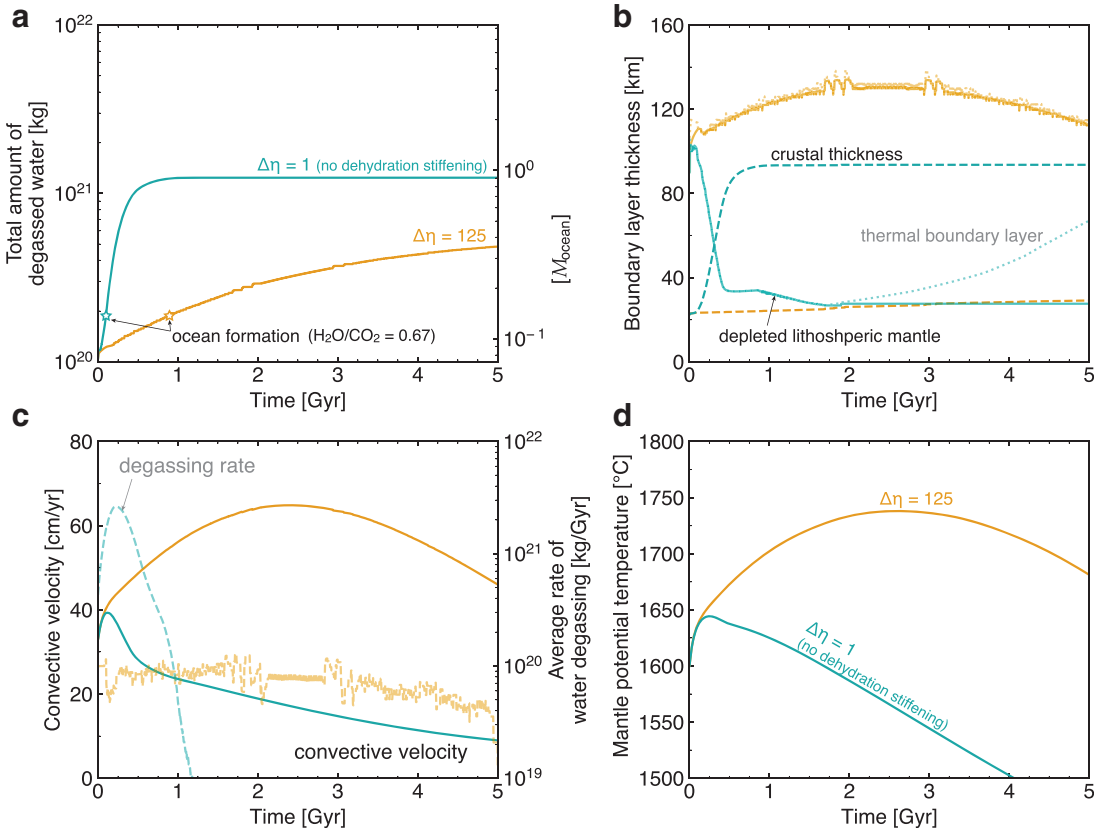

FIG. 7. The same as Figure 6 but for an initial H_2O concentration of 0.04 wt% with two different values for viscosity contrast between dry and wet mantle: $\Delta\eta_w = 1$ (cyan) and 125 (yellow). A larger viscosity contrast results in slower degassing, and thus an oceanless surface would be maintained for a longer time. The case with $\Delta\eta_w = 1$ does not exhibit any dehydration stiffening, and thus convection and mantle degassing are more efficient than the other case, although it is an unrealistic assumption. While DLM is actively eroded by thermal convection and its thickness is kept thin, crust grows rapidly to the point that, after 700 Myr, it becomes thick enough to halt mantle processing [shown in **(c)**]. Markers in **(a)** show the time when a threshold amount of surface H_2O is degassed to stabilize water oceans. Color graphics are available online.

3.2.2. Evolution of super-Earths. For larger planets, the formation of water oceans is predicted only under a restricted range of initial conditions, and even when oceans are expected to emerge, the formation would take longer than Earth-size planets (Fig. 8a). As discussed in Section 2.3, more CO_2 is released during the magma ocean stage on larger planets (Fig. 3b), so a greater amount of surface H_2O is required to stabilize oceans (Fig. 3a). Yet, the amount of water residing at the surface is nearly independent of planetary mass at the beginning of the evolution (Fig. 3a), and the amount of degassed volatiles during solid-state convection increases little with planetary size (Fig. 9). Under the same initial volatile concentrations, larger planets thus may not have a sufficient amount of surface H_2O to stabilize oceans.

Larger planets have a higher rate of degassing, but mantle processing ceases earlier during solid-state convection. This is seen in Fig. 9a, which compares the evolution of surface water for Earth-size and $5M_E$ super-Earth planets: the total amount of degassed water increases faster during the first 1–2 Gyr for a 5 M_E super-Earth, yet no degassing is observed during the subsequent period. The scaling for mantle processing can be derived from Eq. 7:

$$V_{\text{proc}} \sim f_m \Delta t \sim \frac{h_p u_{\text{conv}} r_p^2}{h_{cm}} \Delta t. \tag{15}$$

The scaling for whole mantle convection ($h_{cm} = h_m$) has been provided in O'Rourke and Korenaga (2012) as $V_{\text{proc}} \sim M_p^{0.24} \Delta t$, and a similar scaling for super-Earths can be derived considering the effect of viscous postperovskite in the deeper mantle: h_{cm} decreases to $P_{ppv}/(\rho_m g)$, and u_{conv} to $Ra^{1/2}/h_{cm} \sim (h_{cm} g)^{1/2} \sim 1$. Using the interior model of Valencia *et al.* (2006) ($r_p \sim M_p^{0.26}$) and $h_p \sim g^{-1}$, V_{proc} follow $r_p^2 \Delta t \sim M_p^{0.52} \Delta t$, and degassing is in general more efficient for larger planets during the first 1 Gyr of continuous degassing (Fig. 9).

The duration of degassing, Δt, however, shortens with increasing planetary size. Mantle processing takes space when the initial depth of melting, $h_i = P_i/(\rho_L g)$, is greater than the base of TBL (h_{TBL}), but larger planets are less likely to meet such a condition. When super-Earths of different sizes under the same thermal state are considered, the initial depth of melting scales with g^{-1}, whereas the thickness of the TBL is scaled as

$$h_{\text{TBL}} = \frac{h_{cm}}{Nu} \sim \frac{h_{cm}}{Ra^{1/3}} \sim g^{-1/3}. \tag{16}$$

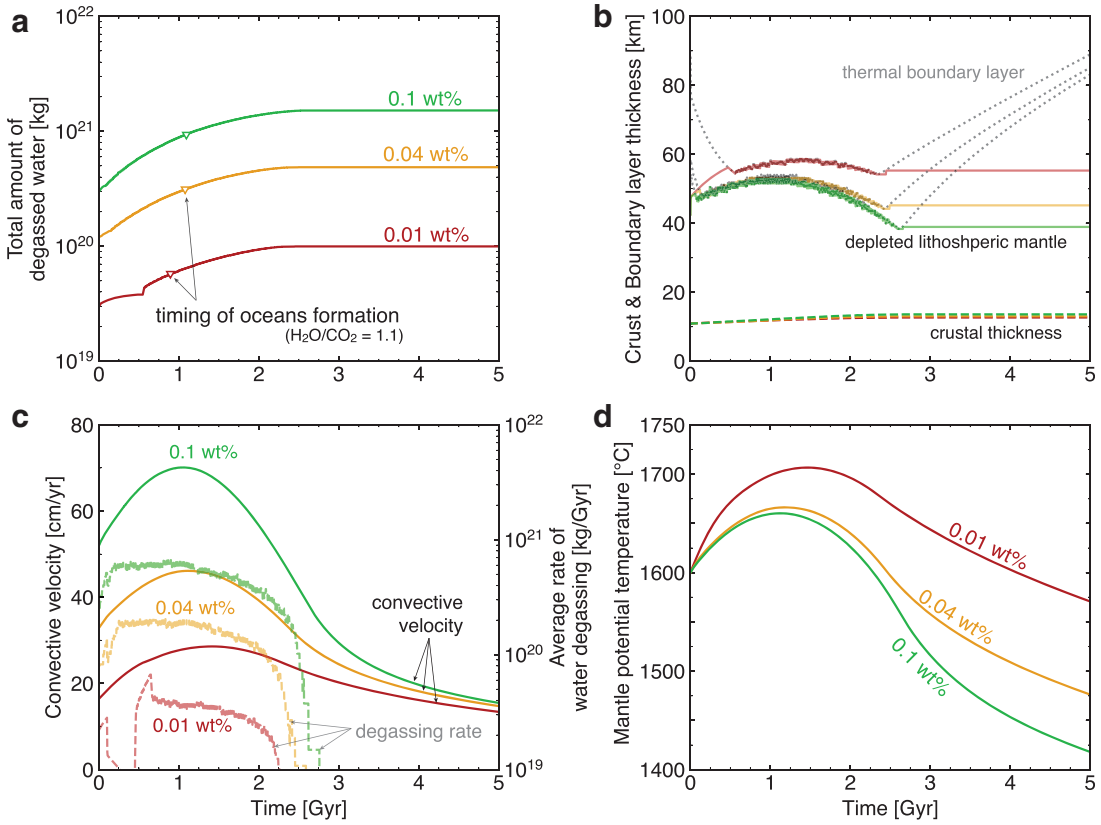

FIG. 8. The thermal evolution and degassing history of $5M_E$ super-Earths under stagnant lid convection. **(a)** Total amount of degassed water; **(b)** thicknesses of crust (dashed), DLM (solid), and TBL (gray); **(c)** convective velocity beneath the lid (solid) and the rate of water degassing averaged over 50 Myr (dashed, light colored); and **(d)** mantle potential temperatures are shown for three different initial H_2O concentrations: 0.01 (red), 0.04 (yellow), and 0.1 wt% (green). Markers in **(a)** show the time when a threshold amount of surface H_2O is degassed to stabilize water oceans, where the H_2O/CO_2 ratio of 1.1 (triangle) and net stellar radiation of 330 W m^{-2} are assumed. For a H_2O concentration of 0.04 wt%, $H_2O/CO_2 = 1.1$ corresponds to $p_{CO_2} \sim 500$ bar, and the total H_2O inventory is 6 ocean masses because the mantle mass of a $5M_E$ super-Earth is ~ 5 times that of Earth. Color graphics are available online.

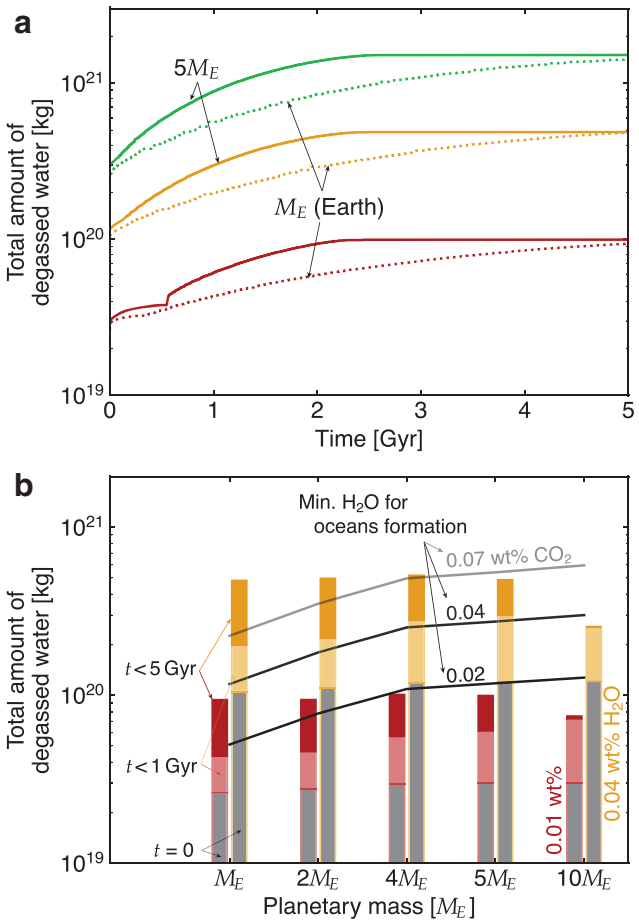

FIG. 9. **(a)** The total amount of degassed water for Earth-size (solid) and $5M_E$ super-Earth planets (dotted) with three different initial H_2O concentrations in the mantle x_{H_2O}: 0.01 (red), 0.04 (yellow), and 0.1 wt% (green). Mantle degassing is faster during the first 1 Gyr but ceases after ~2 Gyr for a $5M_E$ super-Earth. **(b)** The amount of degassed water for different planetary sizes with H_2O concentrations of 0.01 (red) and 0.04 wt% (yellow). The bars show the amount of degassed water during three different periods: before the solidification of a magma ocean (gray), before 1 Gyr (light red/yellow) and 5 Gyr of solid-state convection (dark red/yellow). The minimum amount of surface H_2O for ocean formation is also plotted for initial CO_2 concentrations x_{CO_2} of 0.02 (black), 0.04 (dark gray), and 0.07 wt% (light gray). Color graphics are available online.

With increasing planetary mass, the initial melting depth becomes shallower at a faster rate than TBL and activating mantle processing becomes more difficult. Consequently, mantle processing ceases earlier for larger planets, and even though the rate of mantle degassing is higher during the early stage, the total amount of degassed volatiles throughout their evolution does not change appreciably with planetary size (Fig. 9b). We note that the limited processing of the mantle for larger planets is in a broad agreement with previous studies of two-dimensional (2D) mantle convection models (Dorn *et al.*, 2018). A larger fraction of the water budget is thus expected to remain in the mantle for super-Earths without degassing to the surface, precluding the formation of water oceans.

3.3. Discussion: hydrogen escape and long-term habitability

Hydrogen escape can be important for the timing of ocean formation when the initial H_2O concentration in the mantle (x_{H_2O}) is small and the planet is close to the star. The efficiency of hydrogen escape depends on the mixing ratio of water vapor at the top of the atmosphere, and diffusion is the rate-controlling process when the mixing ratio is below ~2–3%, assuming a similar EUV flux to the present-day Sun and a heating efficiency of 30% (Watson *et al.*, 1981). Although the luminosity of younger stars may be higher than the present-day Sun, hydrogen escape from a planet

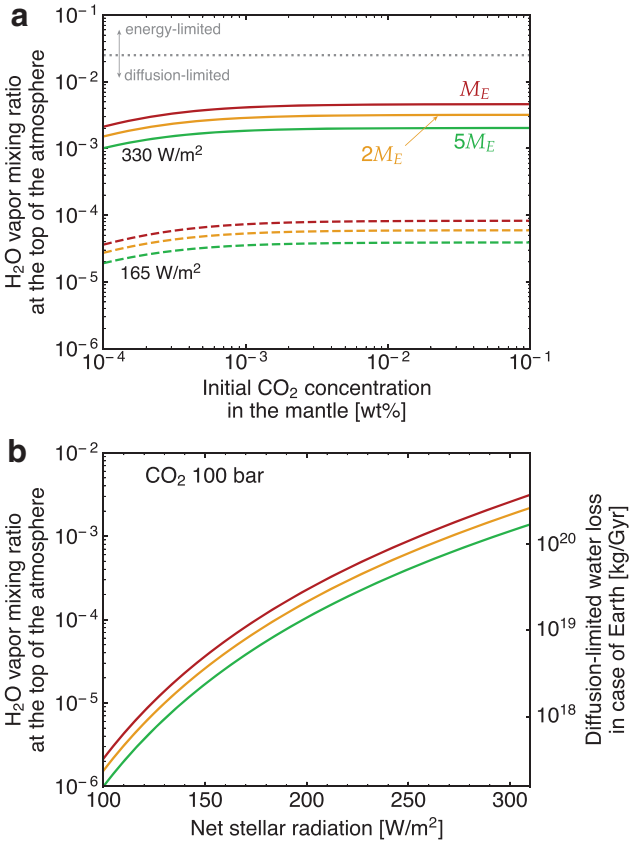

FIG. 10. The mixing ratio of H_2O vapor at the top of the atmosphere as a function of **(a)** the initial CO_2 concentration in the mantle and **(b)** as of net stellar radiation. A planet with water oceans is assumed, and an oceanless one would have a smaller mixing ratio than that shown here. Colors indicate planetary mass: Earth-size (red), $2M_E$ (yellow), and $5M_E$ super-Earth (green). **(a)** Solid and dashed lines represent net stellar radiation of 330 and 165 W m^{-2}, respectively. Dotted gray line describes a critical ratio above which hydrogen escape is limited by the magnitude of EUV flux, and for the range of stellar radiation considered here, hydrogen escape is limited by diffusion. **(b)** An atmosphere containing 1 bar of N_2 and 100 bar of CO_2 is assumed here. Water loss by diffusion-limited hydrogen escape is estimated as well for an Earth-size planet using a binary diffusion coefficient of $b_{H_2} = 1.46 \times 10^{21}$ m^{-1} s^{-1} (Catling and Kasting, 2017). Water is assumed to readily convert to hydrogen at the top of the atmosphere, and thus the values should be treated as an upper bound estimate for water loss. Color graphics are available online.

without a significant envelope would always be limited by diffusion, and thus a larger flux size would not affect the rate of water loss.

The 1D radiative-convective model (Appendix A.2) (Nakajima *et al.*, 1992) predicts that the mixing ratio is <1% for conditions considered in this study (Fig. 10), and thus hydrogen escape would be limited by diffusion (*e.g.*, Catling and Kasting, 2017). For a $5M_E$ super-Earth with a water vapor mixing ratio of 0.003, the total amount of hydrogen escape during a 1 Gyr period could be as large as 4×10^{18} kg, which is equivalent to 4×10^{20} kg of H_2O. This amount is comparable with the total amount of degassed water for $x_{H_2O} < 0.04$ wt% (Fig. 9a), and thus ocean formation would be delayed, or in some case precluded, compared with what is predicted in Figs. 6a and 8a. Diffusion-limited flux is linearly proportional to the mixing ratio, so under a weaker net stellar radiation, the amount of water lost by hydrogen escape is negligible because the atmosphere contains a smaller amount of water vapor (Fig. 10b).

We calculate mantle degassing under solid-state convection and estimate the likelihood and timing of ocean formation at various initial volatile concentrations, considering the loss of water by hydrogen escape. With a stronger net stellar radiation and thus a higher water mixing ratio, hydrogen escape becomes significant and prohibits the formation of ocean formation at a small initial H_2O concentration (x_{H_2O}). On early Venus, for example, if oceans are absent at the time of magma ocean solidification, degassing during solid-state convection does not supply a sufficient amount of water to stabilize oceans, and the surface would lack oceans throughout its evolution under $x_{H_2O} < 0.08$ wt%, equivalent to a total water inventory of $\sim$2.4 ocean mass (Fig. 11a).

Although the threshold x_{H_2O} is higher for larger planets (Fig. 11c), the general trend remains the same. On the contrary, if x_{CO_2} is small and thus water oceans are formed from the beginning, the mantle would operate under plate tectonics, and efficient mantle degassing would maintain oceans during the subsequent period. Therefore, for planets receiving >240 W m^{-2} of radiation with a small initial H_2O content, whether water oceans exist immediately after magma ocean solidification characterizes the long-term existence of water oceans and thus the habitability of planets (Fig. 11).

This could provide an explanation for why Venus and Earth had divergent evolutionary paths: Venus may have continued to lack oceans throughout its history because of the comparable rates of mantle degassing and hydrogen escape, whereas Earth has had water oceans and plate tectonics since the solidification of the mantle surface. The net solar radiation received by early Venus is considered close to the tropospheric radiation limit (Hamano *et al.*, 2013), but even if Venus was not in a runaway greenhouse state, water oceans are not guaranteed on early Venus.

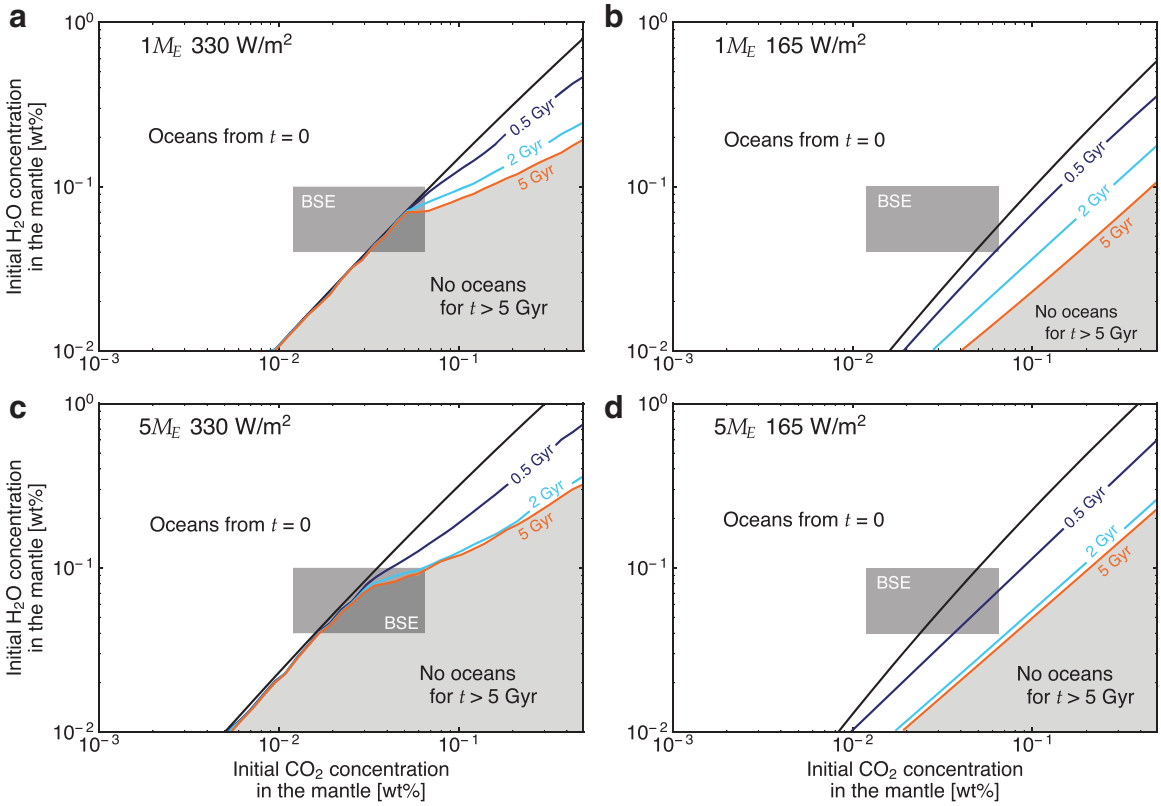

FIG. 11. Contours showing the timing of ocean formation for Earth-size (top; **a, b**) and $5M_E$ super-Earth planets (bottom; **c, d**). Results are calculated for three different levels of net stellar radiation: 330 (left; **a, c**) and 165 W m^{-2} (right; **b, d**). Water oceans form immediately after magma ocean solidification and exist throughout the evolution of planets in regions left of black lines, whereas oceans would be absent for >5 Gyr under conditions shaded in light gray. Rectangles represent the estimated volatile concentrations in the BSE from Hirschmann and Dasgupta (2009) and Korenaga *et al.* (2017). Color graphics are available online.

Limited mantle degassing under stagnant lid convection also implies that the venusian mantle could still be wet and that the amount of hydrogen escape and thus its by-product oxygen could be smaller than previously predicted. Such a small amount of oxygen could be consumed by the oxidation of surface rocks without invoking other removal mechanisms (*e.g.*, Kurosawa, 2015), given that the venusian surface is likely to have continually been resurfaced by magmatism even in the mode of stagnant lid convection (O'Rourke and Korenaga, 2015).

Hydrogen escape has little influence on ocean formation when the stellar radiation is weaker and/or a mantle contains a greater amount of H_2O (Fig. 11b, d). In such cases, planets with the same H_2O/CO_2 ratio would develop water oceans on a similar timescale regardless of the absolute value of initial H_2O concentrations as discussed in Section 3.2.1. For planets resembling early Earth, oceans would exist from the beginning for $H_2O/CO_2>1.5$, and the formation timescale becomes increasingly longer as the H_2O/CO_2 ratio decreases because degassing slows down as the mantle cools (Figs. 6c and 8c; Section 3.2.2).

Degassing eventually discontinues, and thus the surface would never acquire a sufficient amount of water to stabilize oceans for H_2O/CO_2 ratios <0.4. Such threshold ratios for ocean formation increase with planetary mass and net stellar radiation. These values are within the estimate for the BSE (2.4 ± 1.0; Hirschmann and Dasgupta, 2009), so if terrestrial exoplanets have similar volatile concentrations to Earth, the presence of water oceans is not guaranteed, especially for super-Earths. Planets may have a different fate with a slight difference in their volatile concentrations, and the habitability of planets would depend largely on their size and the H_2O/CO_2 ratio of the mantle, in addition to the distance from the central star.

Although its effect is not considered in our study, the rate of hydrogen escape during the magma ocean phase is much higher than that discussed here. A hot surface allows most of the surface water budget to exist as vapor, increasing the mixing ratio at the top of the atmosphere. Because a molten surface only persists for <0.1 Myr in a period after the final giant impact, water loss by hydrogen escape is negligible in the scope of Section 2. Hydrogen escape during the accretionary phase, however, could lead to a significant water loss (Zahnle *et al.*, 1988) and would be important when constraining the water budget of terrestrial planets from the perspective of the chemical composition of planetary building blocks.

4. Discussion and Conclusions

4.1. Additional processes to promote mantle degassing

During the transition from a magma ocean to solid-state convection, we assumed that the solid-dominated layer quickly solidified by the Rayleigh–Taylor instability within the layer. As discussed in Section 2.1, the density structure of the solid-dominated layer is gravitationally unstable, so a newly solidified cold material would continuously be mixed with the pre-existing solid-dominated layer (Maurice *et al.*, 2017). Because the cooling of the surface melt-dominated layer is much faster than the solid-dominated one, the thermal evolution of the solid-dominated layer would mostly be governed by the cold downwelling of newly solidified materials, which is likely to be more efficient than cooling by solid-state convection (Lebrun *et al.*, 2013; Zahnle *et al.*, 2015).

Its effect, however, remains unquantified because its modeling requires the implementation of solidification by adiabatic compression. Viscosity also changes drastically as partially molten materials solidify during the downwelling. Fully incorporating these effects would require some numerical efforts, so we cannot rule out the possibility that the solid-dominated layer remains super adiabatic at the time of surface solidification. In such a case, remaining heat may be released by episodic eruptions, and the amount of surface water could be slightly higher than that predicted in Section 2.

Mantle degassing may also be promoted by tidal heating. It has been suggested that tidal heating inhibits the cooling of a solid-dominated magma ocean (Zahnle *et al.*, 2015), and if the cooling timescale becomes long enough, the percolation of pore melt may transport a significant amount of trapped volatiles to the surface. Quantifying the timescale of mantle cooling, however, is not straightforward. As discussed in the previous paragraph, the cooling of the solid-dominated layer is mostly controlled by the overlying melt-dominated layer, and any heat added by tidal dissipation could efficiently be transported upward by the Rayleigh–Taylor instability within the layer. A simple 1D model would be insufficient to address this complex transition period, and further investigation is warranted. Also, the presence of satellites is not always guaranteed, and even if a satellite exists, its size is not necessarily going to be as large as Earth's moon. The results shown here would thus serve as a baseline understanding on volatile degassing, and we plan to address additional processes in future studies.

4.2. Plate tectonics and the removal of thick CO_2 atmosphere

Plate tectonics maintains a habitable atmospheric composition over geological time (Berner, 2004), so the presence of surface water, a key to plate tectonics, is crucial for the long-term habitability of the planet. Its role is particularly important during the early stage of evolution because most of the CO_2 budget is degassed during magma ocean solidification. When $p_{CO_2} > 100$ bar, its greenhouse effect would maintain a surface temperature >100°C (Abe and Matsui, 1988; Abe, 1993a), which may prevent life forms similar to those that exist on Earth from emerging. The removal of such a thick CO_2 atmosphere likely requires rapid plate motion (Sleep and Zahnle, 2001; Zahnle *et al.*, 2007), so although this study has focused on the formation of water oceans, stabilizing water oceans is only one of the requirements for creating a habitable environment.

The efficiency of CO_2 removal from the atmosphere depends on plate velocity, and when the mantle has a pyrolitic composition, plate velocity could be slower for a hotter mantle than in the present day (Korenaga, 2006, 2010b). Miyazaki and Korenaga (2022) suggest that a chemically heterogeneous mantle resulting from magma oceans solidification (Appendix A.4) would develop a thinner DLM and thus allows faster plate velocity than a pyrolitic mantle. Whether such chemical

differentiation occurs in a solidifying magma ocean is a critical factor in developing a habitable environment, although it depends on several unconstrained physical properties and is subjected to further investigation (Solomatov and Stevenson, 1993; Solomatov *et al.*, 1993; Xie *et al.*, 2020).

Plate velocity also depends strongly on the degree of mantle hydration (Korenaga, 2010b), and the idea of a wet mantle after magma ocean solidification is also consistent with the removal of the thick CO_2 atmosphere. Some previous models of magma ocean degassing have often assumed that the mantle would be entirely dehydrated during solidification (Elkins-Tanton, 2008; Hamano *et al.*, 2013; Lebrun *et al.*, 2013; Salvador *et al.*, 2017), but a dry mantle would have a slower plate motion than in the present day, despite the hotter mantle temperature in the past (Korenaga, 2006). If so, the removal of CO_2 over >100 bar would become highly inefficient (Miyazaki and Korenaga, 2022), which fails to explain the emergence of the moderate climate by the early Archean.

The wet mantle and thus rapid plate motion also agree with recent geochemical modeling, which suggests the efficient recycling of the surface material in the Hadean (Rosas and Korenaga, 2018; Hyung and Jacobsen, 2020). Studies on magma ocean have often suffered from a lack of observational constraints, but we may be able to obtain new insights into this period by taking into account the aftermath of a magma ocean.

4.3. Conclusions

We estimated the likelihood of ocean formation and its timing for planets at various volatile concentrations by solving for the evolution of mantle degassing during and after magma ocean solidification. Considering the rheological transition of a partially molten medium, a magma ocean is predicted to retain a significant fraction of the H_2O inventory, whereas CO_2, which is much less soluble to magma, would mostly reside in the atmosphere after the solidification. When the H_2O/CO_2 ratio is lower than a threshold, surface water exists entirely as water vapor as a result of a strong greenhouse effect, and water oceans would be absent on the surface. Larger planets are less likely to develop water oceans because more greenhouse gases are emitted to the atmosphere during the solidification process.

If water oceans do not form at the beginning of solid-state convection, planets most likely operate under stagnant lid convection, severely limiting mantle degassing during the subsequent evolution. The rate of mantle degassing decreases and eventually reaches zero as the mantle cools and TBL grows, so the majority of H_2O is expected to be retained in the mantle throughout its evolution. The total amount of degassed water is nearly independent of planetary mass under the same volatile concentrations, but because a CO_2 atmosphere is thicker and thus a larger amount of surface water is necessary to form oceans for larger planets, the threshold H_2O/CO_2 ratio for ocean formation increases with planetary size.

The threshold also increases with net stellar radiation as a larger amount of water vapor is contained in the atmosphere. In addition, water loss by hydrogen escape may preclude ocean formation for planets receiving strong radiation and containing a small amount of H_2O. These would not be the case once water oceans form at the surface because the mode of mantle convection would likely change to plate tectonics, promoting mantle degassing during the subsequent evolution.

If the volatile contents of rocky exoplanets are similar to those of the BSE, mantle degassing during magma ocean would not supply a sufficient amount of H_2O when planets are larger and/or receive stronger radiation than Earth. Exoplanets could be richer in volatiles than Earth, and indeed, exoplanets of larger size are known to have an atmosphere of smaller metallicity (Benneke *et al.*, 2019a). Yet, the redox evolution of rocky planets is not well understood, and if hydrogen existed in a reduced form, a high H/C ratio may not necessarily result in the formation of water oceans.

An increasing number of observations for the exoplanet atmosphere are expected with upcoming missions, but the detection of water vapor does not necessarily indicate the presence of water oceans. In addition to the habitable zone, planetary mass and the H_2O/CO_2 ratio are important parameters in predicting the likelihood of oceans on exoplanets. Because the threshold H_2O/CO_2 ratio for ocean formation is lower for smaller planets receiving weaker radiation, such planets are more promising candidates to search for potential life, although they may be more difficult to detect and observe the atmosphere.

Acknowledgments

This article is benefited from the comments by Dan Bower, Darius Modirrousta-Galian, and two anonymous reviewers.

Funding Information

This work was sponsored by the U.S. National Aeronautics and Space Administration under Cooperative Agreement No. 80NSSC19M0069 issued through the Science Mission Directorate and the National Science Foundation under grant EAR-1753916, and in part by the facilities and staff of the Yale University Faculty of Arts and Sciences High Performance Computing Center. Y.M. was supported by the Stanback Postdoctoral Fellowship from Caltech Center for Comparative Planetary Evolution.

Supplementary Material

Supplementary Figure S1

References

Abe Y (1993a) Physical state of the very early Earth. *Lithos* 30: 223–235.

Abe Y (1993b) Thermal evolution and chemical differentiation of the terrestrial magma ocean. *Geophys Monogr* 74:41–54.

Abe Y (1997) Thermal and chemical evolution of the terrestrial magma ocean. *Phys Earth Planet Inter* 100:27–39.

Abe Y and Matsui T (1985) The formation of an impact-generated H_2O atmosphere and its implications for the early thermal history of the Earth. *J Geophys Res* 90:C545–C559.

Abe Y and Matsui T (1988) Evolution of an impact-generated H_2O-CO_2 atmosphere and formation of a hot proto-ocean on Earth. *J Atmos Sci* 45:3081–3101.

Abe Y, Abe-Ouchi A, Sleep NH, *et al.* (2011) Habitable zone limits for dry planets. *Astrobiology* 11:443–460.

Alt JC and Teagle DAH (1999) The uptake of carbon during alteration of ocean crust. *Geochim Cosmochim Acta* 63:1527–1535.

Benneke B, Knutson HA, Lothringer J, *et al.* (2019a) A sub-Neptune exoplanet with a low-metallicity methane-depleted atmosphere and Mie-scattering clouds. *Nat Astron* 3:813–821.

Benneke B, Wong I, Piaulet C, *et al.* (2019b) Water vapor and clouds on the habitable-zone sub-Neptune exoplanet K2-18b. *Astrophys J* 887:L14.

Bercovici D and Ricard Y (2012) Mechanisms for the generation of plate tectonics by two-phase grain-damage and pinning. *Phys Earth Planet Inter* 202–203:27–55.

Bercovici D, Tackley PJ, and Ricard Y (2015) The generation of plate tectonics from mantle dynamics. In *Treatise on Geophysics, Second Edition*, edited by G Schubert, Elsevier B.V., Oxford, UK, Vol. 7, pp 271–318.

Berner RA (2004) *The Phanerozoic Carbon Cycle: CO_2 and O_2*. Oxford University Press, Oxford, UK.

Blank JG and Brooker RA (1994) Experimental studies of carbon dioxide in silicate melts: solubility, speciation, and stable carbon isotope behavior. In *Reviews in Mineralogy and Geochemistry*, edited by MR Carrol and JR Holloway, Mineralogical Society of America, Chantilly, VA, pp 157–186.

Bower DJ, Kitzmann D, Wolf AS, *et al.* (2019) Linking the evolution of terrestrial interiors and an early outgassed atmosphere to astrophysical observations. *Astron Astrophys* 631:A103.

Catling DC and Kasting JF (2017) Escape of atmospheres to space. In *Atmospheric Evolution on Inhabited and Lifeless Worlds*, Cambridge University Press, Cambridge, UK, pp 129–168.

Catling DC and Zahnle KJ (2020) The Archean atmosphere. *Sci Adv* 6:eaax1420.

Davaille A and Jaupart C (1994) Onset of thermal convection in fluids with temperature-dependent viscosity: application to the oceanic mantle. *J Geophys Res* 99:19853–19866.

de Koker N, Karki BB, and Stixrude L (2013) Thermodynamics of the MgO-SiO_2 liquid system in Earth's lowermost mantle from first principles. *Earth Planet Sci Lett* 361:58–63.

Deng J, Du Z, Karki BB, *et al.* (2020) A magma ocean origin to divergent redox evolutions of rocky planetary bodies and early atmospheres. *Nat Commun* 11:2007.

Dorn C, Noack L, and Rozel AB (2018) Outgassing on stagnant-lid super-Earths. *Astron Astrophys* 614:A18.

Dumoulin C, Doin MP, and Fleitout L (1999) Heat transport in stagnant lid convection with temperature- and pressure-dependent Newtonian or non-Newtonian rheology. *J Geophys Res* 104:12759–12777.

Elkins-Tanton LT (2008) Linked magma ocean solidification and atmospheric growth for Earth and Mars. *Earth Planet Sci Lett* 271:181–191.

Elkins-Tanton LT, Parmentier EM, *et al.* (2003) Magma ocean fractional crystallization and cumulate overturn in terrestrial planets: implications for Mars. *Meteorit Planet Sci* 38:1753–1771.

Faul UH and Jackson I (2007) Diffusion creep of dry, melt-free olivine. *J Geophys Res Solid Earth* 112:B04204.

Fraeman AA and Korenaga J (2010) The influence of mantle melting on the evolution of Mars. *Icarus* 210:43–57.

Gardner JE, Hilton M, and Carroll MR (1999) Experimental constraints on degassing of magma: isothermal bubble growth during continuous decompression from high pressure. *Earth Planet Sci Lett* 168:201–218.

Gardner JP, Mather JC, Clampin M, *et al.* (2006) The James Webb Space Telescope. *Space Sci Rev* 123:485–606.

Gerya TV, Connolly JAD, and Yuen DA (2008) Why is terrestrial subduction one-sided? *Geology* 36:43–46.

Gilbert EA, Barclay T, Schlieder JE, *et al.* (2020) The first habitable zone earth-sized planet from TESS. I: validation of the TOI-700 system. *Astrophys J* 160:116.

Gillon M, Triaud AHMJ, Demory B-O, *et al.* (2017) Seven temperate terrestrial planets around the nearby ultracool dwarf star TRAPPIST-1. *Nature* 542:456–460.

Gualda GAR, Ghiorso MS, Lemons RV, *et al.* (2012) Rhyolite-MELTS: aamodified calibration of MELTS optimized for silica-rich, fluid-bearing magmatic systems. *J Petrol* 53:875–890.

Hamano K, Abe Y, and Genda H (2013) Emergence of two types of terrestrial planet on solidification of magma ocean. *Nature* 497:607–610.

Hansen VL (2007) Subduction origin on early Earth: a hypothesis. *Geology* 35:1059–1062.

Hier-Majumder S and Hirschmann MM (2017) The origin of volatiles in the Earth's mantle. *Geochem Geophys Geosyst* 18:3078–3092.

Hirschmann MM (2012) Magma ocean influence on early atmosphere mass and composition. *Earth Planet Sci Lett* 341–344:48–57.

Hirschmann MM and Dasgupta R (2009) The H/C ratios of Earth's near-surface and deep reservoirs, and consequences for deep Earth volatile cycles. *Chem Geol* 262:4–16.

Hirschmann MM, Bergin EA, Blake GA, *et al.* (2021) Early volatile depletion on planetesimals inferred from C–S systematics of iron meteorite parent bodies. *Proc Natl Acad Sci U S A* 118:e2026779118.

Hirth G, Kohlstedt DL (1996) Water in the oceanic upper mantle: implications for rheology, melt extraction and the evolution of the lithosphere. *Earth Planet Sci Lett* 144:93–108.

Hyung E and Jacobsen SB (2020) The $^{142}Nd/^{144}Nd$ variations in mantle-derived rocks provide constraints on the stirring rate of the mantle from the Hadean to the present. *Proc Natl Acad Sci U S A* 117:14738–14744.

Ishiwatari M, Takehiro S-I, Nakajima K, *et al.* (2002) A numerical study on appearance of the runaway greenhouse state of a three-dimensional gray atmosphere. *J Atmos Sci* 59:3223–3238.

Ito E, Harris DM, and Anderson AT (1983) Alteration of oceanic crust and geologic cycling of chlorine and water. *Geochim Cosmochim Acta* 47:1613–1624.

Jain C, Korenaga J, and Karato S (2019) Global analysis of experimental data on the rheology of olivine aggregates. *J Geophys Res Solid Earth* 124:310–334.

Kameyama M, Yuen DA, and Fujimoto H (1997) The interaction of viscous heating with grain-size dependent rheology in the formation of localized slip zones. *Geophys Res Lett* 24:2523–2526.

Kasting JF, Whitmire DP, and Reynolds RT (1993) Habitable zones around main sequence stars. *Icarus* 101:108–128.

Katz RF, Spiegelman M, and Langmuir CH (2003) A new parameterization of hydrous mantle melting. *Geochem Geophys Geosyst* 4:1073.

Kawamoto T and Holloway JR (1997) Melting temperature and partial melt chemistry to H_2O-saturated mantle peridotite to 11 gigapascals. *Science* 276:240–243.

Kite ES, Manga M, and Gaidos E (2009) Geodynamics and rate of volcanism on massive Earth-like planets. *Astrophys J* 700:1732–1749.

Kodama T, Genda H, O'ishi R, *et al.* (2019) Inner edge of habitable aones for Earth-sized planets with various surface water distributions. *J Geophys Res Planets* 124:2306–2324.

Kopparapu RK, Ramirez R, Kasting JF, *et al.* (2013) Habitable zones around main-sequence stars: new estimates. *Astrophys J* 765:131.

Korenaga J (2006) Archean geodynamics and the thermal evolution of Earth. In *Archean Geodynamics and Environments*, edited by K Benn, J-C Mareschal, and K Condie, AGU, Washington, DC, pp 7–32.

Korenaga J (2007) Thermal cracking and the deep hydration of oceanic lithosphere: a key to the generation of plate tectonics? *J Geophys Res* 112:B05408.

Korenaga J (2009) Scaling of stagnant-lid convection with Arrhenius rheology and the effects of mantle melting. *Geophys J Int* 179:154–170.

Korenaga J (2010a) On the likelihood of plate tectonics on super-Earths: does size matter? *Astrophys J* 725:L43–L46.

Korenaga J (2010b) Scaling of plate tectonic convection with pseudoplastic rheology. *J Geophys Res* 115:B11405.

Korenaga J (2017) On the extent of mantle hydration caused by plate bending. *Earth Planet Sci Lett* 457:1–9.

Korenaga J (2020) Plate tectonics and surface environment: role of the oceanic upper mantle. *Earth Sci Rev* 205:103185.

Korenaga J, Planavsky NJ, and Evans DAD (2017) Global water cycle and the coevolution of the Earth's interior and surface environment. *Philos Trans R Soc A* 375: 20150393.

Kurosawa K (2015) Impact-driven planetary desiccation: the origin of the dry Venus. *Earth Planet Sci Lett* 429:181–190.

Lebrun T, Massol H, Chassefière E, *et al.* (2013) Thermal evolution of an early magma ocean in interaction with the atmosphere. *J Geophys Res Planets* 118:1155–1176.

Li J, Bergin EA, Blake GA, *et al.* (2021) Earth's carbon deficit caused by early loss through irreversible sublimation. *Sci Adv* 7:eabd3632.

Lichtenberg T, Bower DJ, Hammond M, *et al.* (2021) Vertically resolved magma ocean–protoatmosphere evolution: H_2, H_2O, CO_2, CH_4, CO, O_2, and N_2 as primary absorbers. *J Geophys Res Planets* 126:e2020JE006711.

Madhusudhan N, Nixon MC, Welbanks L, *et al.* (2020) The interior and atmosphere of the habitable-zone exoplanet K2-18b. *Astrophys J* 891:L7.

Matsui T and Abe Y (1986) Evolution of an impact-induced atmosphere and magma ocean on the accreting Earth. *Nature* 319:303–305.

Maurice M, Tosi N, Samuel H, *et al.* (2017) Onset of solid-state mantle convection and mixing during magma ocean solidification. *J Geophys Res Planets* 122:577–598.

McKenzie D (1984) The generation and compaction of partially molten rock. *J Petrol* 25:713–765.

Mei S and Kohlstedt DL (2000) Influence of water on plastic deformation of olivine aggregates 1. Diffusion creep regime. *J Geophys Res* 105:457–469.

Miyazaki Y and Korenaga J (2019a) On the timescale of magma ocean solidification and its chemical consequences: 1. Thermodynamic database for liquid at high pressures. *J Geophys Res Solid Earth* 124:3382–3398.

Miyazaki Y and Korenaga J (2019b) On the timescale of magma ocean solidification and its chemical consequences: 2. Compositional differentiation under crystal accumulation and matrix compaction. *J Geophys Res Solid Earth* 124:3399–3419.

Miyazaki Y and Korenaga J (2022) A wet heterogeneous mantle creates a habitable world in the Hadean. *Nature* 608: 86–90.

Mojzsis SJ, Harrison TM, and Pidgeon RT (2001) Oxygen-isotope evidence from ancient zircons for liquid water at the Earth's surface 4,300 Myr ago. *Nature* 409:178–181.

Moresi L and Solomatov VS (1998) Mantle convection with a brittle lithosphere: thoughts on the global tectonics styles of the Earth and Venus. *Geophys J Int* 133:669–682.

Nakajima M and Stevenson DJ (2015) Melting and mixing states of the Earth's mantle after the Moon-forming impact. *Earth Planet Sci Lett* 427:286–295.

Nakajima S, Hayashi Y-Y, and Abe Y (1992) A study on the ''runaway greenhouse effect'' with a one-dimensional radiative-convective equilibrium model. *J Atmos Sci* 49: 2256–2266.

Noack L, Rivoldini A, and Van Hoolst T (2017) Volcanism and outgassing of stagnant-lid planets: implications for the habitable zone. *Phys Earth Planet Inter* 269:40–57.

O'Neill C, Marchi S, Zhang S, *et al.* (2017) Impact-driven subduction on the Hadean Earth. *Nat Geosci* 10:793–797.

O'Rourke JG and Korenaga J (2012) Terrestrial planet evolution in the stagnant-lid regime: size effects and the formation of self-destabilizing crust. *Icarus* 221:1043–1060.

O'Rourke JG and Korenaga J (2015) Thermal evolution of Venus with argon degassing. *Icarus* 260:128–140.

Papale P (1997) Modeling of the solubility of a one-component H_2O or CO_2 fluid in silicate liquids. *Contrib Mineral Petrol* 126:237–251.

Pierrehumbert RT and Ding F (2016) Dynamics of atmospheres with a non-dilute condensible component. *Proc R Soc A* 472: 20160107.

Porcelli D and Pepin RO (2000) Rare gas constraints on early Earth history. In *Origin of the Earth and Moon*, edited by RM Canup and K Righter, The University of Arizona Press, Tucson, AZ, pp 435–458.

Quintana EV, Barclay T, Borucki WJ, *et al.* (2016) The frequency of giant impacts on Earth-like worlds. *Astrophys J* 821:126.

Regenauer-Lieb K, Yuen DA, and Branlund J (2001) The initiation of subduction: criticality by addition of water? *Science* 294:578–580.

Rosas JC and Korenaga J (2018) Rapid crustal growth and efficient crustal recycling in the early Earth: implications for Hadean and Archean geodynamics. *Earth Planet Sci Lett* 494: 42–49.

Rubie DC, Jacobson SA, Morbidelli A, *et al.* (2015) Accretion and differentiation of the terrestrial planets with implications for the compositions of early-formed Solar System bodies and accretion of water. *Icarus* 248:89–108.

Salvador A, Massol H, Davaille A, *et al.* (2017) The relative influence of H_2O and CO_2 on the primitive surface conditions and evolution of rocky planets. *J Geophys Res Planets* 122: 1458–1486.

Schulze-Makuch D, Méndez A, Fairén AG, *et al.* (2011) A two-tiered approach to assessing the habitability of exoplanets. *Astrobiology* 11:1041–1052.

Seager S, Kuchner M, Hier-Majumder CA, *et al.* (2007) Mass-radius relationships for solid exoplanets. *Astrophys J* 669: 1279–1297.

Sleep NH and Zahnle K (2001) Carbon dioxide cycling and implications for climate on ancient Earth. *J Geophys Res* 106: 1373–1399.

Solomatov VS (1995) Scaling of temperature and stress dependent viscosity convection. *Phys Fluids* 7:266–274.

Solomatov VS (2007) Magma oceans and primordial mantle differentiation. In *Treatise on Geophysics*, Elsevier B.V., Oxford, UK, Vol. 9, pp 91–119.
Solomatov VS and Moresi L-N (2000) Scaling of time-dependent staganant lid convection: application to small-scale convection on Earth and other terrestrial planets. *J Geophys Res* 105:21795–21817.
Solomatov VS and Stevenson DJ (1993) Suspension in convective layers and style of differentiation of a terrestrial magma ocean. *J Geophys Res* 98:5375–5390.
Solomatov VS, Olson P, and Stevenson DJ (1993) Entrainment from a bed of particles by thermal convection. *Earth Planet Sci Lett* 120:387–393.
Stevenson DJ, Spohn T, and Schubert G (1983) Magnetism and thermal evolution of the terrestrial planets. *Icarus* 54:466–489.
Stixrude L (2014) Melting in super-earths. *Philos Trans R Soc A* 372:20130076.
Tackley PJ, Ammann M, Brodholt JP, *et al.* (2013) Mantle dynamics in super-Earths: post-perovskite rheology and self-regulation of viscosity. *Icarus* 225:50–61.
Tosi N, Godolt M, Stracke B, *et al.* (2017) The habitability of a stagnant-lid Earth. *Astron Astrophys* 605:A71.
Tsiaras A, Waldmann IP, Tinetti G, *et al.* (2019) Water vapour in the atmosphere of the habitable-zone eight-Earth-mass planet K2-18 b. *Nat Astron* 3:1086–1091.
Valencia D, Connell RJO, Sasselov D (2006) Internal structure of massive terrestrial planets. *Icarus* 181:545–554.
van Thienen P (2007) Convective vigour and heat flow in chemically differentiated systems. *Geophys J Int* 169:747–766.
Vilella K and Kaminski E (2017) Fully determined scaling laws for volumetrically heated convective systems, a tool for assessing habitability of exoplanets. *Phys Earth Planet Inter* 266:18–28.
Watson AJ, Donahue TM, and Walker JCG (1981) The dynamics of a rapidly escaping atmosphere: applications to the evolution of Earth and Venus. *Icarus* 48:150–166.
Wilde SA, Valley JW, Peck WH, *et al.* (2001) Evidence from detrital zircons for the existence of continental crust and oceans on the Earth 4.4 Gyr ago. *Nature* 409:175–178.
Xie L, Yoneda A, Yamazaki D, *et al.* (2020) Formation of bridgmanite-enriched layer at the top lower-mantle during magma ocean solidification. *Nat Commun* 11:548.
Zahnle KJ, Kasting JF, and Pollack JB (1988) Evolution of a steam atmosphere during Earth's accretion. *Icarus* 74:62–97.
Zahnle K, Arndt N, Cockell C, *et al.* (2007) Emergence of a habitable planet. *Space Sci Rev* 129:35–78.
Zahnle KJ, Lupu R, Dobrovolskis A, *et al.* (2015) The tethered Moon. *Earth Planet Sci Lett* 427:74–82.

Address correspondence to:
Yoshinori Miyazaki
Division of Geological and Planeatry Sciences
California Institute of Technology
Pasadena, CA 91125
USA

E-mail: ymiya@caltech.edu

Submitted 7 August 2021
Accepted 21 January 2022
Associate Editor: Christopher McKay

Abbreviations Used

1D = one-dimensional
2D = two-dimensional
BSE = bulk silicate Earth
DLM = depleted lithospheric mantle
TBL = thermal boundary layer

Appendix. Method Details

A.1. The Thermal Structure of the Melt-Dominated Layer

Mantle potential temperature, T_m, is calculated to be consistent with the depth of the melt-dominated layer d. The magma ocean is considered to be adiabatic as a result of rapid convection, and T_m is obtained by integrating the adiabatic temperature gradient from the bottom of the melt-dominated layer to the surface (Supplementary Fig. S1). The adiabatic gradient is described as

$$\left(\frac{dT}{dP}\right)_S = \frac{\alpha' T}{\rho c_p'}, \tag{A1}$$

where thermal expansivity, α', and specific heat, c_p', include the effect of phase transition. They are obtained by differentiating the Gibbs free energy of peridotite described in Miyazaki and Korenaga (2019a), and this thermodynamic model is also used to determine other thermodynamic properties, such as density and melt fraction at each depth. The relation between T_m and d for an Earth-size planet is shown in Fig. 2a.

The surface temperature T_s is calculated using a one-dimensional (1D) atmospheric model (Appendix A.2) and depends on the atmospheric mass and composition, calculated from Eqs. 1 to 3, and the net outgoing infrared radiation ($F_\uparrow(\tau = 0)$ in Appendix A.2). The outgoing infrared radiation is the sum of absorbed stellar radiation and convective heat flux, F_{conv}, given by (Zahnle *et al.*, 1988; Solomatov, 2007):

$$F_{\mathrm{conv}} = 0.089 \frac{k(T_m - T_s)}{d} Ra^{1/3}, \tag{A2}$$

where k is thermal conductivity and Ra is the Rayleigh number of the melt-dominated layer. Equation A2 assumes that heat flux from the solid-dominated layer can be ignored because of a much higher viscosity than the melt-dominated one. The Rayleigh number is defined as

$$Ra = \frac{\alpha \rho g (T_m - T_s) d^3}{\kappa \eta_l}, \tag{A3}$$

where α is thermal expansivity, κ is thermal diffusivity, and η_l is the viscosity of the melt-dominated layer. The viscosity η_l does not change significantly until magma experiences rheological transition and thus is set to a constant of 1000 Pa s. The net stellar radiation would be ~ 167 W m^{-2} for the early Earth and ~ 319 W m^{-2} for the early Venus with an albedo of 0.3 and a solar radiation 30% weaker than the present day.

A.2. Atmospheric Model

The surface temperature and the total amount water vapor in the atmosphere are estimated using a 1D radiative-convective model based on Nakajima *et al.* (1992). We consider two layers within the atmosphere: stratosphere and troposphere, where the temperature is controlled by different heat transport mechanism. Whereas radiative equilibrium governs the stratosphere, the thermal structure in the troposphere is characterized by convective heat transport from the bottom. The atmosphere is assumed to be plane-parallel and is transparent to stellar radiation, but it is opaque to infrared radiation regardless of the wavelength. Although this assumption of gray atmosphere may underestimate the surface temperature during the earlier stage of magma ocean, the calculated temperatures are similar for the gray and nongray cases for surface temperatures below 200°C (Salvador *et al.*, 2017). For simplicity, the effects of clouds are neglected in our model.

The thermal profile of the stratosphere can be written as a function of optical thickness, τ:

$$\sigma_B T(\tau)^4 = \frac{1}{2} F_{\rm net}\left(\frac{3}{2}\tau + 1\right), \tag{A4}$$

where σ_B is the Stefan-Boltzmann constant and $F_{\rm net}$ is the net infrared flux emitted from the top of the atmosphere. Upward, $F_\uparrow$, and downward radiation fluxes, $F_\downarrow$, are also calculated as

$$F_\uparrow(\tau) = \frac{1}{2} F_{\rm net}\left(\frac{3}{2}\tau + 2\right), \tag{A5}$$

$$F_\downarrow(\tau) = \frac{1}{2} F_{\rm net}\left(\frac{3}{2}\tau\right). \tag{A6}$$

Optical thickness τ is defined so that it increases toward Earth's surface:

$$\tau(z) = -\int_\infty^z \kappa \rho_g dz. \tag{A7}$$

Opacity, κ, depends on the atmospheric concentrations of greenhouse gases, and for the atmosphere which has a molar fraction of x_i of gas species i, κ is given by

$$\kappa = \frac{1}{\bar{\mu}} \sum_i \kappa_i x_i \mu_i, \tag{A8}$$

where $\bar{\mu}$ is the mean molar mass of gas, κ_i and μ_i are the opacity and molar mass, respectively, of species i. For an infrared absorption coefficient, we use 10^{-2} for H_2O, 1.3×10^{-4} for CO_2, and 0 for N_2 (Abe and Matsui, 1985). All species are assumed to be transparent to stellar radiation, and thus the downward radiation $F_\downarrow$ is set to 0 at $\tau = 0$. The composition of the atmosphere is considered to be uniform in the stratosphere.

In the troposphere, the thermal structure is controlled by the moist adiabatic lapse rate, which is described as

$$\frac{dT}{dP} = \frac{\bar{\mu}}{\rho_g C_p} \frac{1 + \frac{qL}{RT}}{1 + \frac{qL^2}{C_p R T^2}}, \tag{A9}$$

where ρ_g is the mean gas density, C_p is heat capacity, q is water mixing ratio, and L is the latent heat of the water. Water mixing ratio q is set to be saturated, which is likely in a CO_2 dominated atmosphere, and is obtained from the water phase diagram. Although the moist adiabatic lapse rate is derived assuming a completely saturated atmosphere, we assume that relative humidity in the troposphere is fixed at a value smaller than 1 (*e.g.*, Nakajima *et al.*, 1992).

The tropopause, a boundary between the stratosphere and troposphere, is determined as a height that the radiation energy is balanced. The upward radiation flux emitted from the troposphere can be calculated as

$$F_\uparrow(\tau) = -\sigma_B T^4 + \int_{\tau_b}^{\tau} e^{-(\tau'-\tau)} \frac{d}{d\tau'}\left(\sigma_B T(\tau')^4\right) d\tau', \tag{A10}$$

where τ_b is the optical depth at the bottom of the atmosphere. We assume that the upward flux at the ground is the blackbody radiation of the ground temperature ($F_{\uparrow,\,\rm surf} = -\sigma_B T_{\rm surf}^4$). At the optical depth of the tropopause, τ_p, the values of $F_\uparrow(\tau_p)$ calculated from Eqs. A5 and A10 should be identical to satisfy the energy balance. We search for the profiles of temperature and water vapor content that agree with energy conservation. The temperature and the water vapor mixing ratio are smoothly connected at the tropopause.

A.3. The Initial Thickness of Depleted Lithospheric Mantle

The thickness of the partial melt layer when the melt-dominated layer disappears (Fig. 5) is estimated based on an adiabatic temperature profile with a critical melt fraction of 0.4 at the surface. The timescale for the Rayleigh–Taylor instability is predicted to be faster than the rate of solidification (Maurice *et al.*, 2017; Miyazaki and Korenaga, 2019b), and thus the upper mantle is likely to have an adiabatic thermal gradient when the surface of the mantle solidifies. The partial melt layer would experience degassing by percolation, so the bottom pressure of the partial melt layer also becomes the initial base pressure of depleted lithospheric mantle (DLM) (Section 3.1.2).

The adiabatic gradient is expressed as (Mckenzie, 1984):

$$\left(\frac{dT}{dP}\right)_S = \phi \frac{\alpha_l T}{\rho_l c_{p,l}} + (1-\phi)\frac{\alpha_s T}{\rho_s c_{p,s}} - \frac{T\Delta S}{c_p}\left(\frac{d\phi}{dP}\right)_S, \tag{A11}$$

where c_p is specific heat per unit mass and ΔS is entropy change upon melting. Subscripts l and s denote the melt and liquid phases, respectively. Values adopted for thermal expansivity are 3.0 and 4.6×10^{-5} K^{-1} for α_s and α_l, and, for density, ρ_l and ρ_s are taken to be 2900 and 3300 kg m^{-3}, respectively. We adopt 1000 J kg^{-1} K^{-1} for c_p and 300 J kg^{-1} K^{-1} for ΔS. Melt fraction at a given temperature and pressure is calculated using the Rhyolite-MELTS model (Gualda *et al.*, 2012), and the term $d\phi/dP$ in Eq. A11 is calculated so that changes in T and ϕ are consistent with thermodynamics.

A.4. Mantle Composition After Magma Ocean Solidification

The depth of the partial melt layer and the thickness of DLM depend on the mantle composition after magma ocean solidification, which could be different from the present-day mantle as a result of differentiation (Elkins-Tanton *et al.*, 2003; Maurice *et al.*, 2017; Miyazaki and Korenaga, 2019b). We assume a homogeneous pyrolitic mantle in this study, but if the mantle experiences differentiation during magma ocean, Miyazaki and Korenaga (2019b) suggests that the mantle would develop a chemically heterogeneous structure, consisting of high-Mg# pyroxenite and Fe-rich blobs. The settling and sedimentation of a liquidus mineral (Mg-rich bridgmanite; de Koker *et al.*, 2013) at the base of the melt-dominated layer produces a lower mantle comprised of high-Mg# and SiO_2-rich materials, whereas the upper mantle is left with residual Fe-rich dense materials. This structure is gravitationally unstable and is subject to small-scale Rayleigh–Taylor instabilities with a length scale shorter than 100 km. Fe-rich blobs may break down by some degree during the downwelling, but because of high solid viscosity, the two components are unlikely to be completely homogenized in a short period. At the end of solidification, Fe-rich materials would thus have existed as small blobs embedded in a high-Mg# pyroxenite matrix.

The Rhyolite-MELTS model suggests that such a pyroxenite would be mostly dehydrated at $\sim$2 GPa under a mantle potential temperature of 1600°C (see Extended Data figure 1 in Miyazaki and Korenaga, 2022 for details). On the contrary, a homogeneous pyrolytic mantle becomes dehydrated by $\sim$5 GPa under the same mantle potential temperature. This is because the high-Mg# pyroxenite has lower FeO and CaO contents and lacks low-solidus minerals including clinopyroxene and plagioclase. Decompressional melting would thus start at a shallower depth for the chemically heterogeneous mantle, and the amount of volatiles degassed by percolation (Figs. 2–4) is expected to be smaller than that of a pyrolitic mantle. The long-term evolution of surface water (Figs. 6–9), however, would not be significantly different between these two cases because the chemically heterogeneous mantle should be homogenized after some time. The solidus temperature would decrease as high-Mg# pyroxenite and Fe-rich blobs are mixed, and thus the amount of surface water would quickly increase and eventually become similar to the case of a pyrolitic mantle.

Appendix References

Abe Y and Matsui T (1985) The formation of an impact-generated H_2O atmosphere and its implications for the early thermal history of the Earth. *J Geophys Res* 90:C545–C559.

de Koker N, Karki BB, and Stixrude L (2013) Thermodynamics of the MgO-SiO_2 liquid system in Earth's lowermost mantle from first principles. *Earth Planet Sci Lett* 361: 58–63.

Elkins-Tanton LT, Parmentier EM, and Hess PC (2003) Magma ocean fractional crystallization and cumulate overturn in terrestrial planets: implications for Mars. *Meteorit Planet Sci* 38:1753–1771.

Gualda GAR, Ghiorso MS, Lemons RV, *et al.* (2012) Rhyolite-MELTS: aamodified calibration of MELTS optimized for silica-rich, fluid-bearing magmatic systems. *J Petrol* 53:875–890.

Maurice M, Tosi N, Samuel H, *et al.* (2017) Onset of solid-state mantle convection and mixing during magma ocean solidification. *J Geophys Res Planets* 122:577–598.

Mckenzie D (1984) The generation and compaction of partially molten rock. *J Petrol* 25:713–765.

Miyazaki Y and Korenaga J (2019a) On the timescale of magma ocean solidification and its chemical consequences: 1. Thermodynamic database for liquid at high pressures. *J Geophys Res Solid Earth* 124:3382–3398.

Miyazaki Y and Korenaga J (2019b) On the timescale of magma ocean solidification and its chemical consequences: 2. Compositional differentiation under crystal accumulation and matrix compaction. *J Geophys Res Solid Earth* 124:3399–3419.

Miyazaki Y and Korenaga J (2022) A wet heterogeneous mantle creates a habitable world in the Hadean. *Nature* 608: 86–90.

Nakajima S, Hayashi Y-Y, and Abe Y (1992) A study on the ''runaway greenhouse effect'' with a one-dimensional radiative-convective equilibrium model. *J Atmos Sci* 49: 2256–2266.

Salvador A, Massol H, Davaille A, *et al.* (2017) The relative influence of H_2O and CO_2 on the primitive surface conditions and evolution of rocky planets. *J Geophys Res Planets* 122: 1458–1486.

Solomatov VS. (2007) Magma oceans and primordial mantle differentiation. In *Treatise on Geophysics*, Elsevier B.V., Oxford, UK, Vol. 9, pp 91–119.

Zahnle KJ, Kasting JF, and Pollack JB (1988) Evolution of a steam atmosphere during Earth's accretion. *Icarus* 74: 62–97.